MOLECULAR BIOLOGY

Thermostable small-molecule inhibitor of angiogenesis and vascular permeability that suppresses a pERK-FosB/ΔFosB–VCAM-1 axis

Yue Li[1], Ahmad M. N. Alhendi[1], Mei-Chun Yeh[1], Mina Elahy[1], Fernando S. Santiago[1], Nandan P. Deshpande[2], Ben Wu[1], Enoch Chan[1], Shafqat Inam[1], Leonel Prado-Lourenco[1], Jessica Marchand[3], Rohan D. Joyce[3], Lorna E. Wilkinson-White[4], Mark J. Raftery[5], Meidong Zhu[6,7,8], Samuel J. Adamson[8], François Barnat[9], Karen Viaud-Quentric[9], Jim Sockler[10], Joel P. Mackay[11], Andrew Chang[7,8,12], Paul Mitchell[13], Sebastian M. Marcuccio[3,14], Levon M. Khachigian[1]*

Vascular permeability and angiogenesis underpin neovascular age-related macular degeneration and diabetic retinopathy. While anti-VEGF therapies are widely used clinically, many patients do not respond optimally, or at all, and small-molecule therapies are lacking. Here, we identified a dibenzoxazepinone BT2 that inhibits endothelial cell proliferation, migration, wound repair in vitro, network formation, and angiogenesis in mice bearing Matrigel plugs. BT2 interacts with MEK1 and inhibits ERK phosphorylation and the expression of FosB/ΔFosB, VCAM-1, and many genes involved in proliferation, migration, angiogenesis, and inflammation. BT2 reduced retinal vascular leakage following rat choroidal laser trauma and rabbit intravitreal VEGF-A_{165} administration. BT2 suppressed retinal CD31, pERK, VCAM-1, and VEGF-A_{165} expression. BT2 reduced retinal leakage in rats at least as effectively as aflibercept, a first-line therapy for nAMD/DR. BT2 withstands boiling or autoclaving and several months' storage at 22°C. BT2 is a new small-molecule inhibitor of vascular permeability and angiogenesis.

INTRODUCTION

Vascular permeability and neovascularization are hallmark features of macular edema in diabetic retinopathy (DR) and neovascular (wet/exudative) age-related macular degeneration (nAMD) (*1*, *2*). Retinal vascular permeability is triggered by endothelial activation and dysfunction causing breakdown of the blood-retinal barrier (*3*) and interstitial edema through increased osmotic pressure (*4*) and is regulated by mediators such as vascular endothelial growth factor (VEGF), originally known as vascular permeability factor (*5*). All current approved targeted therapies for nAMD and DR rely on VEGF and include bevacizumab/Avastin [humanized monoclonal antibody (hMAb) targeting VEGF-A; Genentech], ranibizumab/Lucentis (VEGF-A hMAb; Genentech/Novartis), and aflibercept/VEGF-Trap/Eylea (fusion protein comprising extracellular domains of VEGF-R1/2 fused to Fc; Regeneron/Bayer). In patients with diabetic macular edema (DME) with poor initial visual acuity, aflibercept is most effective at improving vision (*6*). Aflibercept use for retinal disease is rapidly increasing in the United States and is the third costliest drug subsidized by the Australian Government ($AU304.4 million in 2017–2018) (*7*). Approximately one in four patients with nAMD (*8*) and one in three with DME (*9*) do not optimally respond to existing therapy. Alternative approaches to those solely targeting VEGF are needed.

Transcription factors, particularly those encoded by immediate-early genes, integrate pathologic cues from the extracellular environment with changes in gene expression. One such factor is activator protein 1 (AP-1), a family of proteins belonging to the Fos (c-Fos, FosB, Fra1, and Fra2) and Jun (c-Jun, JunB, and JunD) families (*10*). AP-1 has been implicated in the pathogenesis of retinal disease (*11*, *12*), as have cytokine agonists of AP-1 [e.g., interleukin-1β (IL-1β) (*13*)], kinases upstream [e.g., extracellular signal–regulated kinase (ERK) (*14*)], and genes downstream [e.g., vascular cell adhesion molecule–1 (VCAM-1) (*15*, *16*)]. AP-1 components are highly expressed in epiretinal membranes of patients with proliferative DR compared with controls (*17*). AP-1 can mediate the migratory and proliferative effects of VEGF (*18*) and binds the VEGF promoter at $^{-1139}$TGAATCA^{-1123} (*19*). FosB and ΔFosB are both encoded by the *FosB* gene. ΔFosB lacks the C-terminal 101 amino acids present in FosB because of alternative splicing; is more stable than FosB; and plays a well-established role in drug addiction, stress, and antidepressant response (*20*). AP-1 has been the subject of drug discovery programs, but no inhibitors have been approved. Here, we used a high-throughput screening (HTS) strategy to identify a dibenzoxazepinone that blocks a pERK-FosB/ΔFosB-VCAM-1 axis, inhibits endothelial activation, suppresses angiogenesis, reduces retinal permeability, and retains biological activity even after boiling or autoclaving.

[1]Vascular Biology and Translational Research, School of Medical Sciences and UNSW Medicine, University of New South Wales, Sydney, NSW 2052, Australia. [2]Systems Biology Initiative, School of Biotechnology and Biomolecular Sciences, University of New South Wales, Sydney, NSW 2052, Australia. [3]Advanced Molecular Technologies Pty Ltd, Scoresby, VIC 3179, Australia. [4]Sydney Analytical Core Facility, University of Sydney, NSW 2006, Australia. [5]Bioanalytical Mass Spectrometry Facility, University of New South Wales, Sydney, NSW 2052, Australia. [6]New South Wales Tissue Bank, New South Wales Organ and Tissue Donation Service, South Eastern Sydney Local Health District, Kogarah, NSW 2217, Australia. [7]Save Sight Institute, Discipline of Clinical Ophthalmology and Eye Health, University of Sydney, NSW 2006, Australia. [8]GreenLight Clinical Pty. Ltd., Woolloomooloo, NSW 2011, Australia. [9]Iris Pharma, La Gaude 06610, France. [10]Statistical Operations and Programming, Datapharm Australia Pty. Ltd., Drummoyne, NSW 2047, Australia. [11]School of Life and Environmental Sciences, University of Sydney, NSW 2006, Australia. [12]Sydney Eye Hospital, Sydney NSW 2000 and University of Sydney, NSW 2006, Australia. [13]Centre for Vision Research, Department of Ophthalmology, Westmead Institute for Medical Research, Westmead Hospital, University of Sydney, Westmead, NSW 2145, Australia. [14]La Trobe Institute for Molecular Science, La Trobe University, Melbourne, VIC 3086, Australia.
*Corresponding author. Email: l.khachigian@unsw.edu.au

RESULTS

Identification of BT2, T4, and T6

To identify novel small-molecule inhibitors of AP-1, we screened the ~100,000 compound Walter and Eliza Hall Institute of Medical Research (WEHI) Lead Discovery Library using a 293 cell-based assay in which Firefly luciferase was driven by multiple copies of the AP-1 response element. A substructure filter was applied during the course of the screening to remove pan-assay interference compounds (PAINS) (*21*) that typically capture the AP-1 inhibitor curcumin (*22*). This yielded 24 available hits with an IC_{50} (median inhibitory concentration) in the micromolar or submicromolar range determined using 11-point titration curves, including the dibenzoxazepinone BT2. This followed an earlier screen of a 960 compound DIVERSet library (ChemBridge) that yielded the benzophenone Cpd B/X/LK001 (fig. S1A). T4, T6, and T7 are structural analogs of Cpd B/X/LK001, whereas BT3 is an analog of BT2 (Table 1). BT2 was synthesized subsequent to the screen by reacting commercially available 2-amino-10-ethyldibenzo[b,f][1,4]oxazepin-11 (10H)-one (BT3) with diethyl pyrocarbonate (fig. S1B, scheme 1). Cpd B/X/LK001 was produced by reacting 2-methoxyethyl carbonisocyanatidate (2) (*23*) with the commercially available (4-aminophenyl)(4-chlorophenyl) methanone (1) (fig. S1B, scheme 4). Treatment of Cpd B/X/LK001 with hydroxylamine hydrochloride gave T4 as a ~1:1 mixture of E and Z isomers (fig. S1B, scheme 4). Flubendazole (T6) and (4-aminophenyl)(4-fluorophenyl)methanone (T7) were commercially sourced.

BT2, T4, and T6 inhibit serum-inducible endothelial FosB/ΔFosB and c-Fos expression and block proliferation, migration, and network formation in vitro

We determined the effect of BT2, T4, and T6 on the serum-inducible expression of two different AP-1 subunits in cultured human microvascular endothelial cells (HMEC-1). Endothelial cells provide a vital barrier between the flowing blood and tissue that become hyperpermeable when activated or stressed. BT2 blocked the inducible expression of FosB and ΔFosB (Fig. 1A, top, and fig. S2A, top). T4 and T6 inhibited less potently, while BT3 and T7 demonstrated no inhibition (Fig. 1A). BT2 also blocked the inducible expression of c-Fos, a known mediator of angiogenesis (Fig. 1A, bottom, and fig. S2A, bottom) (*24*).

We next investigated the effects of these compounds on endothelial cell growth using the xCELLigence System that monitors cell proliferation in real time. We found that BT2, T4, and T6 each inhibited serum-inducible proliferation at concentrations in a dose-dependent manner (Fig. 1B). In contrast, BT3 or T7 had no inhibitory effect. To confirm that growth inhibition was not merely due to cell death, we tested one of these compounds (BT2) in a whole-cell proliferation assay in which the Countess system is coupled with trypan blue exclusion. BT2 inhibited serum-inducible proliferation without affecting trypan blue incorporation (fig. S2B). In the dual chamber Transwell system, BT2, T4, and T6 inhibited migration of bovine aortic endothelial cells (BAECs) toward VEGF-A_{165} in serum-containing medium (Fig. 1C). BAECs were used for this purpose since HMEC-1 cells lack VEGFR-2 (Flk/KDR) and only weakly migrate toward VEGF (*25*). BAECs, on the other hand, express VEGFR-2 (*26*) and migrate to VEGF-A (*27*). In contrast, neither BT3 nor PD98059 [allosteric mitogen-activated protein kinase (MAPK) kinase (MEK) inhibitor], imatinib (tyrosine kinase inhibitor), or tofacitinib (Janus kinase inhibitor) had an inhibitory effect at the same concentration (Fig. 1C).

Endothelial cell repair after mechanical injury in vitro evokes a proliferative and migratory response. BT2, T4, and T6 blocked this reparative response within 48 hours, whereas BT3 or T7 had no such effect (Fig. 1D). We also evaluated the effect of these compounds in an endothelial network formation assay (also known as tubule formation) atop reconstituted basement membrane matrix typically used to characterize angiogenic factors and processes (*28*). Endothelial cells in this assay form capillary-like networks maximally within a few hours and regress thereafter. BT2, T4, and T6 inhibited network formation at 2, 4, 6, and 24 hours (Fig. 1E).

BT2 prevents retinal vascular permeability and angiogenesis

Since retinal vascular permeability is a key pathologic feature in nAMD and DME/DR (*29*), we sought to determine the effect of BT2, T4, and T6 on fluorescein leakage induced in eyes of Brown Norway pigmented rats after multiple laser burns of Bruch's membrane around the optic nerve. BT2 (192 μg) reduced retinal permeability by ~50%, an effect similar to aflibercept/Eylea [200 μg administered six times (days 0, 3, 7, 10, 14, and 17) by intravitreal injection over 21 days as compared with two injections (days 0 and 7) of BT2] or triamcinolone acetonide (200 μg intravitreally, day 0; Kenacort) (Fig. 2A). In contrast, T4 and T6, delivered as per BT2, had no inhibitory effect (Fig. 2A). Aflibercept is a first-line therapy for nAMD and DME in the United States, Europe, and Asia Pacific, while Kenacort is a corticosteroid commonly used to treat DME. BT2 also reduced the vascular permeability induced by recombinant human VEGF-A_{165} (rhVEGF-A_{165}) in pigmented rabbits causing fluorescein leakage. Single intravitreal delivery of BT2 (600 μg) inhibited retinal leakage after 2 days by ~50% (Fig. 2B). Immunohistochemical staining of lasered rat eyes 21 days after injury revealed that BT2 inhibited inducible CD31 staining in the inner plexiform layer (IPL) and inner nuclear layer (INL) (Fig. 2C and fig. S3A), where CD31 is expressed after laser injury (*30*). BT2 also inhibited the inducible expression of VEGF-A_{165} (Fig. 2D), consistent with findings of VEGF expression mainly in the outer retina (*31*, *32*). VEGF-A_{165} stained in a gradient relative to the wound that was inhibited by BT2 (Fig. 2E). The murine Matrigel plug assay confirmed the anti-angiogenic properties of BT2. Matrigel containing VEGF-A_{165}, heparin, and compound was subcutaneously implanted to C57BL/6 mice, and CD31 staining in plugs after 7 days was quantified. BT2 suppressed new blood vessel formation, whereas BT3 had no effect (Fig. 2F and fig. S3B).

BT2 inhibits ERK phosphorylation, FosB/ΔFosB, and VCAM-1 expression

Endothelial cells exposed to IL-1β undergo rapid ERK phosphorylation. IL-1β causes endothelial cell permeability (*33*) and retinal leukostasis (*34*). Diabetics with macular edema have higher concentrations of IL-1β among other cytokines and VEGF in the aqueous humor (*35*). We used IL-1β as a model agonist with HMEC-1 in Western blotting experiments. BT2 inhibited IL-1β–inducible ERK phosphorylation, FosB/ΔFosB, and VCAM-1 expression (Fig. 3A and fig. S4). BT2 inhibition of VCAM-1 was further demonstrated by flow cytometry (Fig. 3B and fig. S5).

RNA sequencing (RNA-seq) affirmed BT2's ability to suppress IL-1β–inducible FosB and VCAM-1 expression (Fig. 3C). From a pool of 33,379 gene IDs, there were 325 genes induced by IL-1β twofold or more [log fold change (FC) $\geq$ 2], 89 (27.5%) of which were inhibited by BT2 (logFC $\geq$ 2) (table S1). Principal components

Table 1. Characteristics of BT2 and Cpd X/B/LK001 and their analogs. N/A, not applicable.

Compound	Chemical name	Chemical formula	Molecular weight (Da)	Class	CAS no.	Chemical structure
BT2	(10-Ethyl-11-oxo-10,11-dihydro-dibenzo[b,f][1,4] oxazepin-2-yl)-carbamic acid ethyl ester	$C_{18}H_{18}N_2O_4$	326.35	Dibenzoxazepinone	CAS 922029-50-3	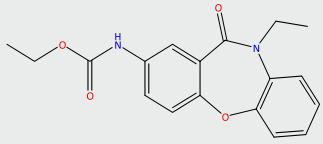
BT3	2-Amino-10-ethyldibenzo[b,f] [1,4] oxazepin-11 (10H)-one	$C_{15}H_{14}N_2O_2$	254.28	Dibenzoxazepinone	CAS 23474-61-5	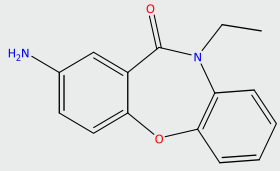
CpdX CpdB LK001	2-Methoxyethyl[[[4-(4-chlorobenzoyl)phenyl] amino]carbonyl] carbamate	$C_{18}H_{17}ClN_2O_5$	376.79	Benzophenone	351068-74-1	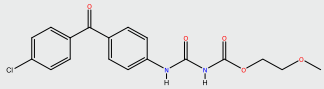
T4	2-Methoxyethyl[[[4-(4-chlorophenyl) (hydroxyimino)methyl) phenyl]amino]carbonyl] carbamate	$C_{18}H_{18}ClN_3O_5$	391.81	Benzophenone	N/A	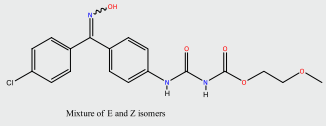 Mixture of E and Z isomers
T6	Flubendazole	$C_{16}H_{12}FN_3O_3$	313.28	Benzophenone	CAS 31430-15-6	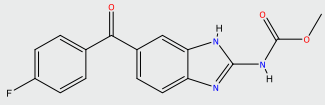
T7	(4-Aminophenyl) (4-fluorophenyl) methanone	$C_{13}H_{10}FNO$	215.22	Benzophenone	CAS 10055-40-0	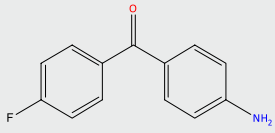
BT2-MeOA	*N*-(10-ethyl-11-oxo-10,11-dihydrodibenzo[b,f][1,4] oxazepin-2-yl)-2-methoxyacetamide	$C_{18}H_{18}N_2O_4$	326.35	Dibenzoxazepinone	CAS 922029-59-2	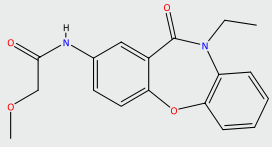
BT2-EOMe	Ethyl (10-(2-methoxyethyl)-11-oxo-10,11-dihydrodibenzo[b,f][1,4] oxazepin-2-yl)carbamate	$C_{19}H_{20}N_2O_5$	356.37	Dibenzoxazepinone	N/A	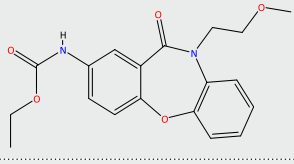
BT2-Pr	Ethyl (11-oxo-10-propyl-10,11-dihydrodibenzo[b,f] [1,4]oxazepin-2-yl) carbamate	$C_{19}H_{20}N_2O_4$	340.37	Dibenzoxazepinone	CAS 922029-50-3	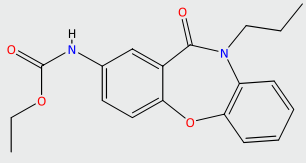
BT2-IC	Isobutyl (10-ethyl-11-oxo-10,11-dihydrodibenzo[b,f] [1,4]oxazepin-2-yl) carbamate	$C_{19}H_{20}N_2O_4$	340.37	Dibenzoxazepinone	N/A	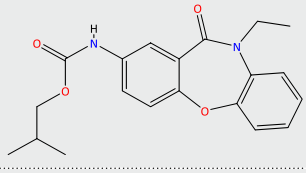

Continued on next page

BT2-IMO	Ethyl (11-(oxetan-3-ylmethoxy)dibenzo[b,f][1,4]oxazepin-2-yl) carbamate	$C_{20}H_{20}N_2O_5$	368.38	Dibenzoxazepinone	N/A	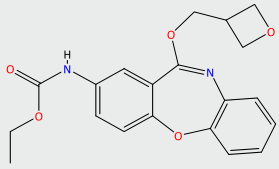
BT2-MO	Ethyl (10-(oxetan-3-ylmethyl)-11-oxo-10,11-dihydrodibenzo[b,f][1,4]oxazepin-2-yl)carbamate	$C_{20}H_{20}N_2O_5$	368.38	Dibenzoxazepinone	N/A	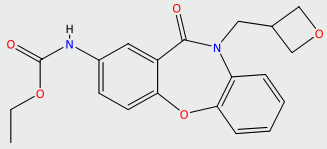
BT2-deut	Ethyl (10-ethyl(2′,2′,2′-d3)-11-oxo-10,11-dihydrodibenzo[b,f][1,4]oxazepin-2-yl)carbamate	$C_{18}H_{15}D_3N_2O_4$	329.37	Dibenzoxazepinone	N/A	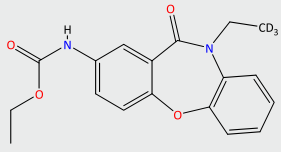

analysis (PCA) (Fig. 3C, top left) showed close association between biological replicates. BT2 also inhibited a range of other regulatory genes involved in cell proliferation, migration, angiogenesis, and inflammation including intercellular adhesion molecule–1 (ICAM-1), CXCL2, KLF5, Egr-1, and Fos (Fig. 3C, with ontologies represented in figs. S6, A to D).

Dose escalation and Western blotting experiments revealed that BT2 inhibited VCAM-1 and ERK phosphorylation more potently than PD98059 (Fig. 3D and fig. S7A). In contrast, BT2, like PD98059, had no effect on IL-1β–inducible phospho–stress-activated protein kinase/c-Jun N-terminal kinase (p-SAPK/JNK) or phospho-p38 (p-p38) (fig. S7B). To explore the hitherto unrecognized dependence of VCAM-1 expression upon FosB/ΔFosB, we performed small interfering RNA (siRNA) knockdown experiments. FosB siRNA inhibited both FosB/ΔFosB and VCAM-1, whereas VCAM-1 siRNA inhibited VCAM-1 but not FosB/ΔFosB (Fig. 3E). Overexpression of ERK1 did not increase levels of phosphorylated ERK compared with IL-1β stimulation, nor did it increase levels of FosB, ΔFosB or VCAM-1 (fig. S7C). Similarly, overexpression of FosB or ΔFosB did not increase VCAM-1 expression compared with IL-1β stimulation (fig. S7C). These findings indicate that, in this agonist-free system where ERK is not phosphorylated, FosB and VCAM-1 are not directly activated by ERK1 overexpression, nor is VCAM-1 directly activated by FosB or ΔFosB overexpression. These data complement our demonstration (under conditions of agonist stimulation) that BT2, which prevents ERK phosphorylation, abrogates the induction of FosB/ΔFosB and VCAM-1 in vitro (Fig. 3, A to D) and in vivo (Fig. 4, A to E). BT2 physically interacts with MEK1 (Fig. 5C), which phosphorylates ERK. These findings, together with our demonstration that IL-1β induction of VCAM-1 is blocked with FosB siRNA (Fig. 3E), suggest that while FosB is necessary for cytokine-inducible VCAM-1 expression, FosB overexpression alone is not sufficient to induce VCAM-1 without cytokine stimulation. FosB likely relies on cofactors (or posttranslational modifications) under conditions of cytokine stimulation.

Immunohistochemical staining of rat retinas revealed that BT2 suppressed inducible pERK staining in the INL, outer plexiform layer (OPL), and outer nuclear layer (ONL) (Fig. 4A), consistent with pERK expression in this proximity (*36*, *37*). BT2 also inhibited retinal FosB immunostaining (Fig. 4B). Moreover, BT2 reduced inducible VCAM-1 expression in the outer limiting membrane (OLM) (Fig. 4C) where others have found that VCAM-1 is expressed (*38*). BT2 also inhibited FosB (Fig. 4D and fig. S3C) and VCAM-1 (Fig. 4E) immunoreactivity in Matrigel plugs.

In further experiments, we compared the biological potency of BT2 with curcumin in the endothelial network formation assay. While BT2 abolished network formation at 1 μM after 4 hours, no inhibition was observed with curcumin at this concentration (figs. S8, A and B). Curcumin appeared to inhibit network formation at 30 μM by ~25% and 40 μM by ~50% (fig. S8B), indicating that BT2 is >40-fold more potent than curcumin in this assay.

BT2 structural analogs lack the biological potency of BT2

We next explored whether the biological potency or solubility of BT2 could be improved by structural modification. Dibenzoxazepinones are typically poorly soluble in water. Six BT2 analogs (aside from BT3) were generated (BT2-MeOA, BT2-EOMe, BT2-Pr, BT2-IC, BT2-MO, and BT2-IMO) (Table 1). BT2-MeOA was synthesized by coupling methoxyacetic acid with 2-amino-10-ethyldibenzo[b,f][1,4]oxazepin-11 (10H)-one (BT3), while BT2-IC was synthesized using the diisobutyl dicarbonate (fig. S1B, scheme 1). BT2-Pr and BT2-EOMe were synthesized from commercially available (1) and (2) (fig. S1B, scheme 2) with the same protocol used to prepare BT2. A tri-deuterated derivation of BT2 was synthesized for stability analysis by alkylating 2-nitro-10H-dibenzo[b,f][1,4]oxazepin-11-one (3) with d_3-iodoethane followed by reduction of the nitro group to give compound (4) (fig. S1B, scheme 3). This intermediate was reacted with diethyl pyrocarbonate to give the desired product. Alkylation of 2-nitro-10H-dibenzo[b,f][1,4]oxazepin-11-one (3) with oxetan-3-ylmethyl methanesulfonate gave both O- and N-alkylated products in 13 and 48% yield, respectively, after column chromatography (fig. S1B, scheme 3). The O- and N-alkylated products were reduced to give the corresponding anilines (5) and (6) (fig. S1B, scheme 3) and then converted in the usual manner

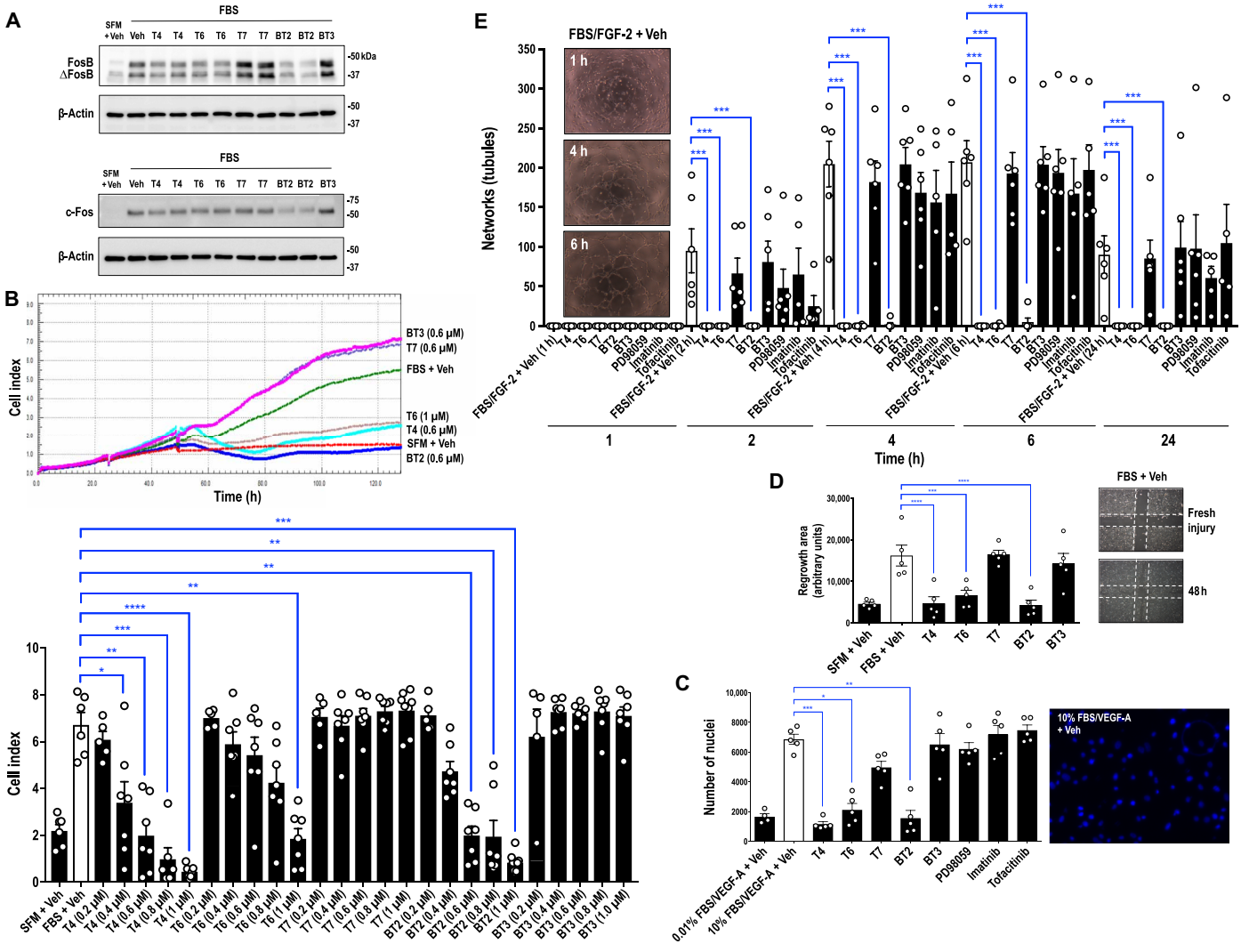

Fig. 1. BT2, T4, and T6 block endothelial FosB/ΔFosB expression, proliferation, migration and wound repair after in vitro injury and network formation. (**A**) HMEC-1 cells were serum-arrested for 20 hours, treated with 30 μM compound in serum-free medium (SFM) (without EGF/hydrocortisone) for 4 hours, and stimulated with 10% fetal bovine serum (FBS) (with EGF/hydrocortisone) and compound (same concentration) for 1 hour. Western blotting was then performed with independent biological duplicates where indicated. Approximate positions of molecular weight markers are shown. Data represent three biologically independent experiments. Veh, vehicle. (**B**) Serum-deprived HMEC-1 cells were treated with compound in 5% FBS (with EGF/hydrocortisone), and proliferation was monitored using xCELLigence. Top: Representative real-time profiles from one experiment. Cell index is a quantitative measure of cell growth. Bottom: Data represent means ± SEM of five to eight independent experiments after 79 hours. One-way analysis of variance (ANOVA). (**C**) BAECs in 10% FBS were seeded into wells containing 0.8-μm Transwell inserts. After 48 hours, medium was changed to 0.01% FBS for 48 hours. Compounds (1 μM) were added to the upper chamber in 0.01% FBS, and medium in the lower chamber was changed to 10% FBS and VEGF-A_{165} (50 ng/ml). Cells were left for 24 hours. Typical 4′,6-diamidino-2-phenylindole–stained nuclei are shown. Nuclei were quantified with National Institutes of Health (NIH) ImageJ. Data represent means ± SEM of four to five independent experiments. Kruskal-Wallis multiple comparisons test. (**D**) Scraped HMEC-1 monolayers were treated with 0.6 μM compound in 5% FBS. Regrowth in denuded area was measured 48 hours after scraping. Representative regrowth from one experiment is shown. Regrowth area was determined with Image-Pro Plus. Data represent means ± SEM of five independent experiments. One-way ANOVA. (**E**) HMEC-1 cells in 1% FBS and fibroblast growth factor 2 (FGF-2; 50 ng/ml) were mixed with compound (3 μM) and seeded in wells coated with Matrigel. Network formation over 24 hours was quantified using Image-Pro Plus. Data represent means ± SEM of five to six independent experiments. Kruskal-Wallis multiple comparisons test. Representative network formation on Matrigel from same control well over time is shown. Where indicated, *P < 0.05, **P < 0.01, ***P < 0.001, ****P < 0.0001.

using diethyl pyrocarbonate to the target products BT2-IMO and BT2-MO.

Dilution of these compounds in medium containing serum revealed that only one of these analogs (BT2-MeOA) had greater solubility than BT2 and that BT3 was the most soluble of all these dibenzoxazepinones (fig. S9A). Adding serum to the diluent increased BT2 solubility (fig. S9B), consistent with reports that serum albumin can increase the dissolution of unionizable drugs (*39*). Neither BT2-MeOA nor any other BT2 analog had the ability to inhibit serum-inducible proliferation (Fig. 5A) or network formation on Matrigel (Fig. 5B) as, or more potently than, BT2. BT2-IC showed some inhibition of network formation at higher concentrations (fig. S9D).

Since BT2 suppressed ERK phosphorylation, we hypothesized that BT2 may interact with MEK1 or MEK2. Binding of BT2 and PD98059 to recombinant His-MEK1 or His-MEK2 was tested by surface plasmon resonance (SPR). Over the concentration range

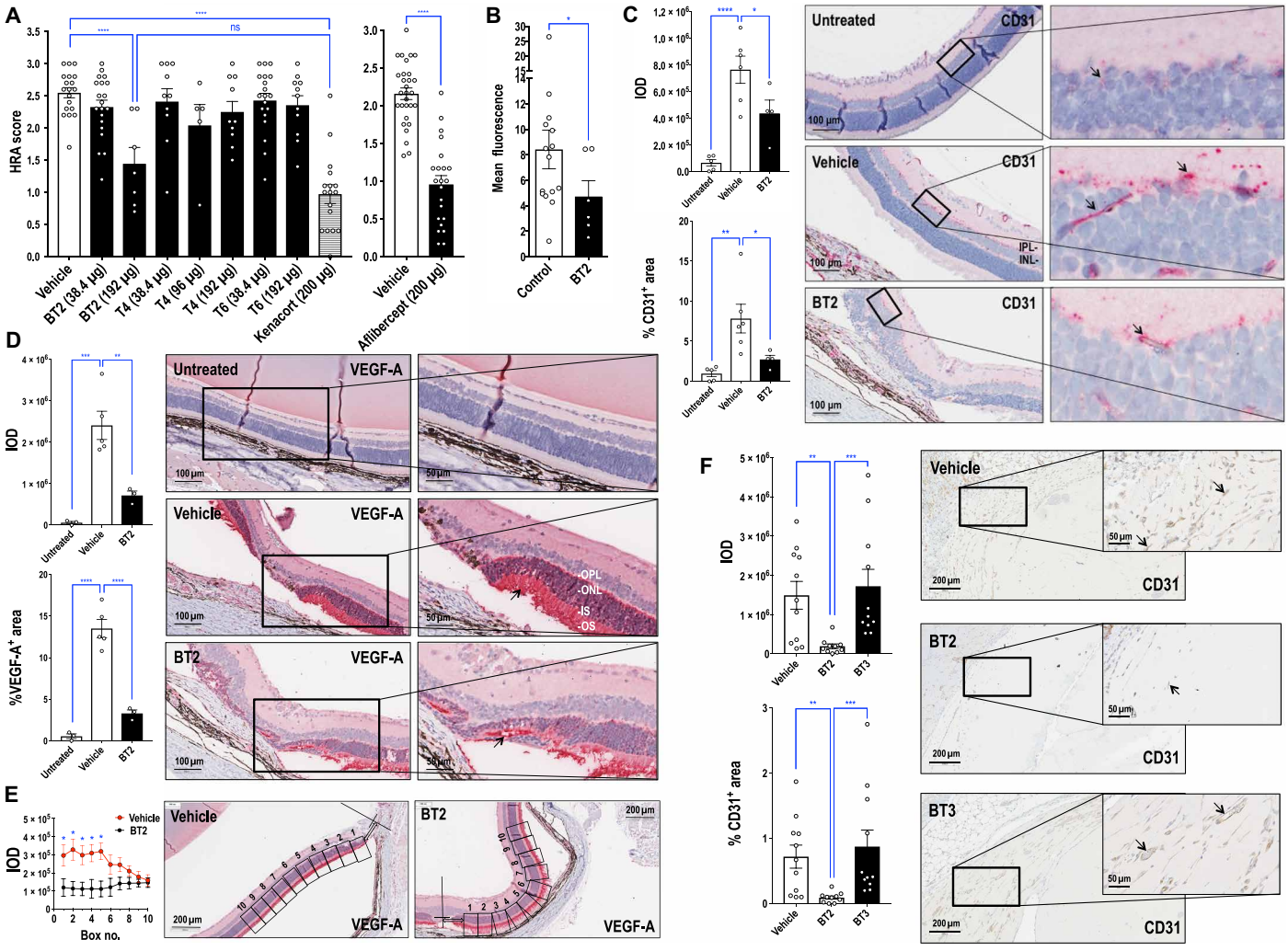

Fig. 2. BT2 inhibits retinal vascular permeability and inhibits CD31, VEGF-A_{165}, pERK, FosB/ΔFosB, and VCAM-1. (**A**) Compound or vehicle (control) was injected intravitreally in rat eyes twice, Kenacort once, and Aflibercept/Eylea six times following six laser burns of retina. On days 14 and 21, sodium fluorescein was subcutaneously injected. After 10 min, ocular fluorescence was recorded using Heidelberg retinal angiography (HRA) and scored, combining days 14 and 21 data. Data represent means ± SEM. One-way ANOVA (plot at left) or *t* test (plot at right and BT2 versus Kenacort in plot at left). $n = 5$ to 29 per group. (**B**) Compound (600 µg) or vehicle was injected intravitreally into the right (R) eyes of rabbits 5 days before intravitreal injection of 500 ng of rhVEGF-A_{165} in 50 µl in same eyes. After 2 days, sodium fluorescein was injected intravenously, and after 1 hour, ocular fluorescence measured in R and left (L) eyes and expressed as ratio (*R*/*L*) for each rabbit. Ratio data from vehicle and BT3 groups pooled (control) as both conditions were inactive and did not differ statistically, for comparison with BT2. Data represent means ± SEM. *t* test, $n = 6$ to 8 per group. Immunohistochemical staining in rat retinal lesions for (**C**) CD31, (**D**) VEGF-A_{165}, and (**E**) VEGF-A_{165} in 100-µm boxed increments relative to wound. Untreated refers to eyes not lasered or injected. Slides photographed under 10× or 20× objective and magnified views are shown. $n = 4$ to 6 per group for CD31, $n = 3$ to 6 per group for VEGF-A_{165}, or $n = 3$ to 5 per group for VEGF-A_{165} gradient analysis. Data represent means ± SEM of mean/animal. One-way ANOVA, Mann-Whitney, or *t* test, as appropriate. Arrows indicate positive staining. (**F**) Matrigel (500 µl) containing VEGF-A_{165} (100 ng/ml), heparin (10 U), and compound (2.5 mg per mouse) or vehicle injected subcutaneously into left flanks of mice. Plugs after 7 days stained for CD31. Representative images under 10× objective with inset providing magnified view (40×). Data represent means ± SEM of mean/animal. Kruskal-Wallis multiple comparisons test. $n = 10$ to 11 per group. ns, not significant; IOD, integrated optical density; OPL, outer plexiform layer; ONL, outer nuclear layer. Where indicated, *$P < 0.05$, **$P < 0.01$, ***$P < 0.001$, ****$P < 0.0001$.

able to be assayed, BT2 bound to His-MEK1 better than to His-MEK2 (Fig. 5C, bottom). In contrast and as expected, PD98059 is bound to both His-MEK1 and His-MEK2 (Fig. 5C, middle) (*40*). Over equivalent concentration ranges, there was no appreciable binding of BT3, BT2-MeOA, or BT2-Pr to either MEK1 or MEK2 (Fig. 5C, top). BT2-IC showed some interaction with MEK1 (but not MEK2). The drop-off in interaction at higher concentrations is possibly due to BT2-IC insolubility [limit of solubility, 8 ± 2 µM, determined by ^{1}H one-dimensional (1D) nuclear magnetic resonance (NMR) spectroscopy]. Western blotting revealed that BT2-IC inhibited both ERK phosphorylation (fig. S9C) and network formation (fig. S9D) at 3 µM (albeit less potently than BT2) but not at 1 µM (Fig. 5, B and D).

BT2 retains stability and biological potency after sonication and 100°C treatment or autoclaving

Last, in considering the potential pharmaceutical appeal of BT2, we explored whether this compound [as a sonicated preparation in saline containing 0.01% dimethyl sulfoxide (DMSO) and 0.5%

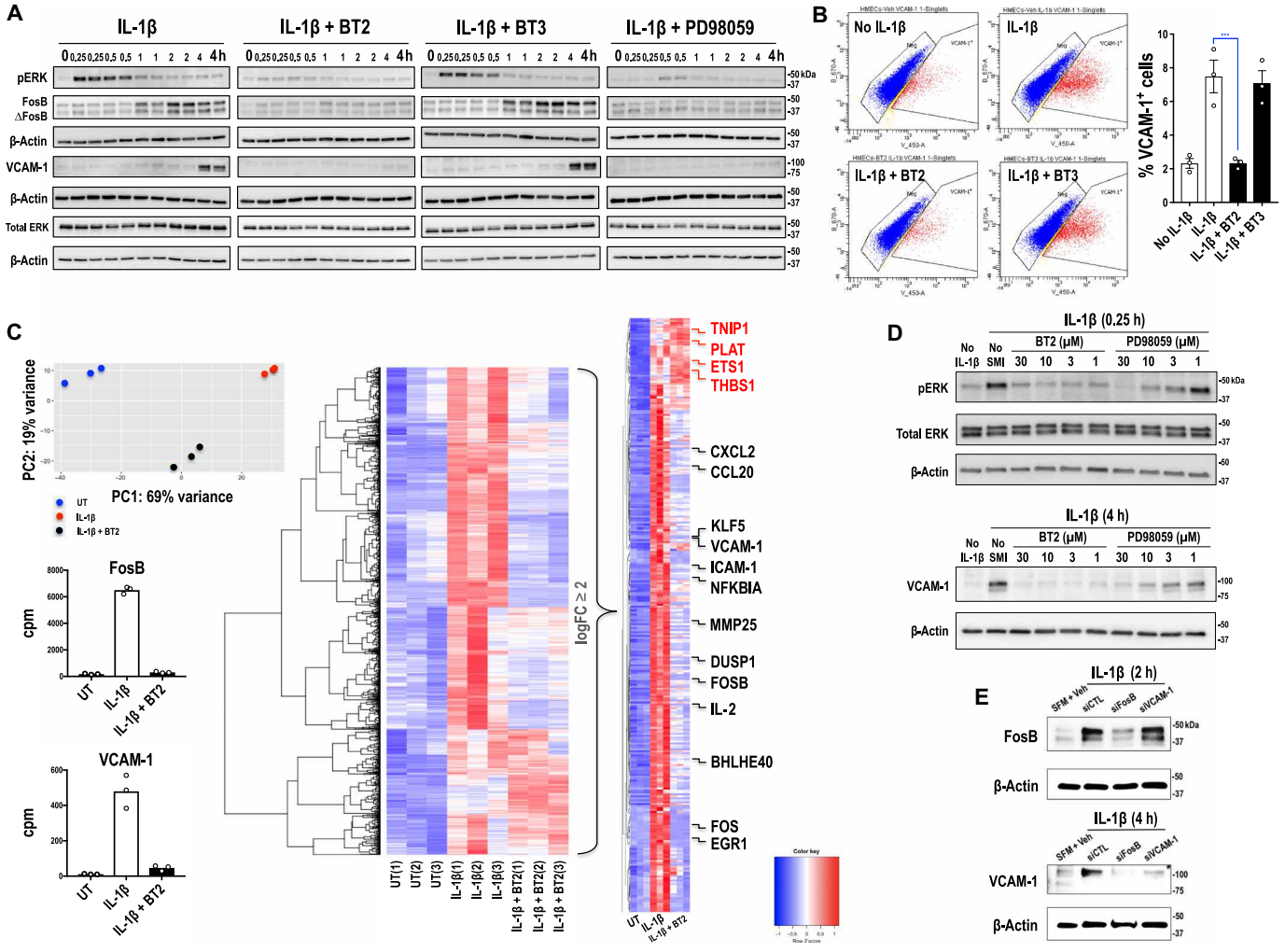

Fig. 3. BT2 inhibits ERK phosphorylation, FosB/ΔFosB, and VCAM-1 expression. (**A**) HMEC-1 cells treated with 30 μM compound were stimulated with IL-1β (20 ng/ml) for times indicated. Western blots representative of two to three biologically independent experiments each performed with two biologically independent replicates run in separate lanes (where shown). (**B**) Flow cytometry performed with HMEC-1 treated with 30 μM compound and IL-1β (20 ng/ml) for 4 hours. Data represent means ± SEM of three independent experiments. One-way ANOVA. $n = 3$ per group. (**C**) RNA-seq performed with total RNA prepared from HMEC-1 pretreated with 30 μM BT2 and IL-1β (20 ng/ml) for 4 hours. PCA plot (top left) shows close association between biological replicates within untreated (UT), IL-1β, and IL-1β + BT2 and clear separation across conditions. Heat map (center, 1579 genes) was generated for all up-regulated genes for comparison of IL-1β versus UT. Counts per million (cpm) values used and genes (rows) grouped using hierarchical clustering with cpm for FosB and VCAM-1 are plotted. Heat map (right) shows 325 genes with logFC ≥ 2. FosB, c-Fos, and VCAM-1 are indicated in the figure together with other genes inhibited by BT2. The figure also shows small subset of genes (in red) further induced by BT2. (**D**) BT2 inhibits IL-1β–inducible VCAM-1 expression and ERK phosphorylation more potently than PD98059. Concentrations of BT2 and PD98059 (1 to 30 μM) indicated. Data represent three biologically independent experiments. SMI, small molecule inhibitor. (**E**) HMEC-1 treated with 0.6 μM siRNA then stimulated with IL-1β (20 ng/ml) for 2 or 4 hours. Western blotting was performed with indicated antibodies. Data are representative of two biologically independent experiments. Approximate positions of molecular weight markers are shown. Where indicated, ***$P < 0.001$.

Tween 80] retained biological potency and stability after extreme heat treatment. Rapid resolution liquid chromatography–tandem mass spectrometry (RRLC-MS/MS) revealed that BT2 remains stable with or without heat treatment (100°C for 10 min) and 6 weeks of storage at 22°C, with only 0.2 and 1% discrepancy in BT2 content in non–heat-treated and heat-treated formulations, respectively (fig. S10A). BT2 retained its ability to inhibit serum-inducible endothelial proliferation under these conditions (fig. S10B). Even more unexpectedly, there was no loss in biological efficacy or degradation even up to 16 months (fig. S10, C and D). The BT2 formulation remained stable and biologically active 4 months after standard autoclaving and storage at 22°C (fig. S10E). Antibodies and other proteins, which comprise all current nAMD/DME drugs, are typically inactivated by extreme heat (*41*).

DISCUSSION

New therapeutic approaches complementing existing VEGF-based strategies for nAMD/DR are needed (*5*). While intravitreal anti-VEGF remains first-line therapy for retinal leakage, alternative therapies are required, as many patients do not optimally respond or the response is not sustained. The Comparison of AMD Treatments Trials study with 647 nAMD patients treated with ranibizumab or bevacizumab showed that vision gains during the first 2 years

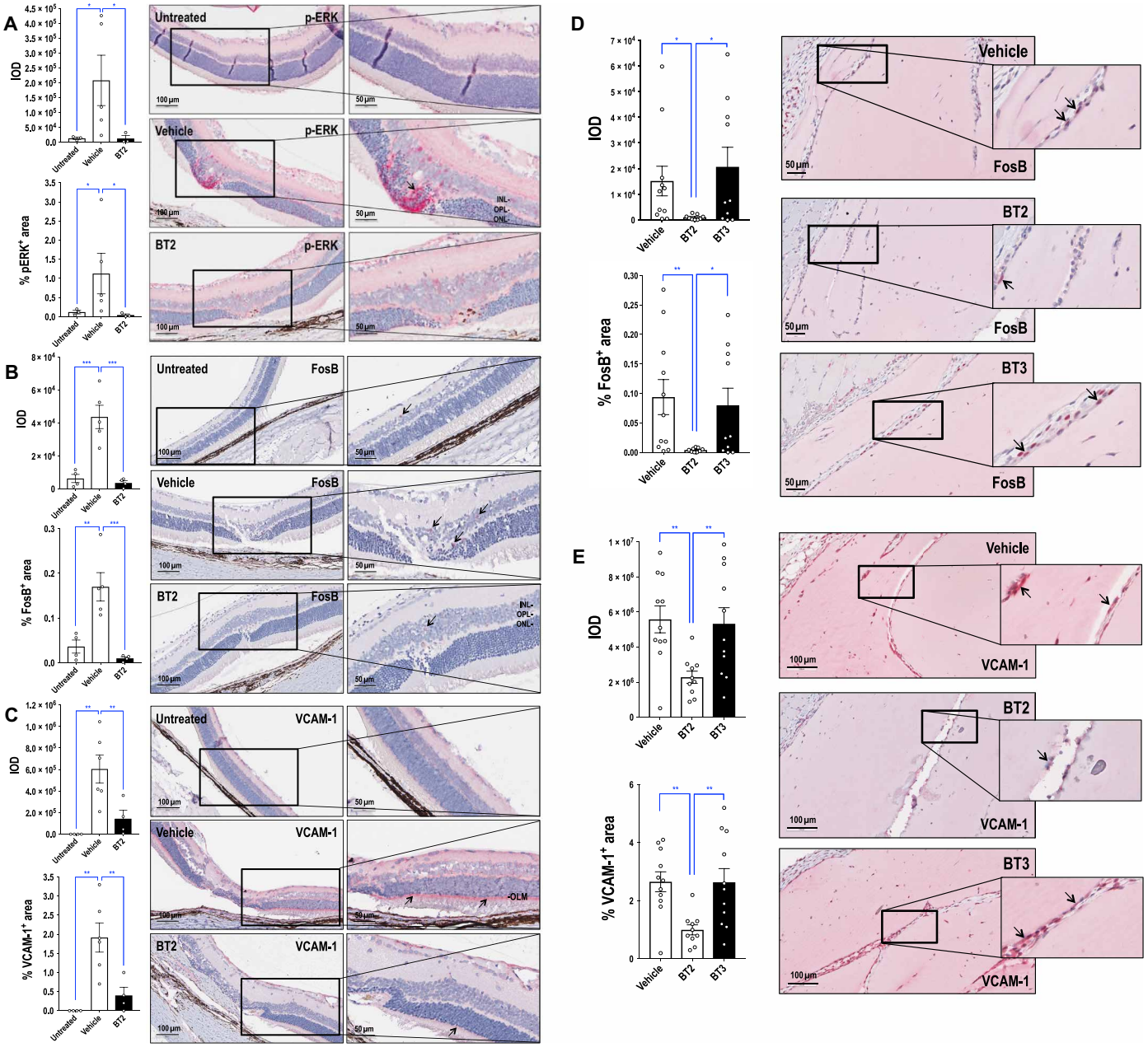

Fig. 4. BT2 inhibits ERK phosphorylation, FosB/ΔFosB, and VCAM-1 expression in retinas and Matrigel plugs. Immunohistochemical staining in retinal lesions was performed for (**A**) pERK, (**B**) FosB, and (**C**) VCAM-1. IOD of positive staining (red chromogen) was assessed using Image-Pro Plus software. Slides were photographed under 20× or 40× objective, and magnified views are shown. $n = 3$ to 5 per group for pERK and FosB and $n = 4$ to 6 per group for VCAM-1. Data represent means ± SEM of the mean/animal. Statistical significance was assessed by one-way ANOVA, Kruskal-Wallis, Mann-Whitney, or *t* test, as appropriate. Arrows provide examples of positive staining. Alternatively, Matrigel plugs were stained for (**D**) FosB or (**E**) VCAM-1. Representative FosB or VCAM-1 staining was photographed under 40× or 20× objective, respectively, with the inset providing a magnified view. Staining was quantified using Image-Pro Plus software. Data represent means ± SEM. Statistical significance was assessed by Kruskal-Wallis multiple comparisons test (FosB, $n = 9$ to 11 per group) or one-way ANOVA (VCAM-1, $n = 10$ to 11 per group). Arrows provide examples of positive staining. Where indicated, $^*P < 0.05$, $^{**}P < 0.01$, $^{***}P < 0.001$.

were not maintained at 5 years (*42*, *43*). The AURA[iv] study of 2227 nAMD patients in eight European countries also revealed that while anti-VEGF therapy resulted in initial improvement in visual acuity, gains were not maintained over time and declined, mainly because of undertreatment (*44*).

Here, we report our discovery and biological characterization of a novel dibenzoxazepinone from a high-throughput screen of ~100,000 compounds. BT2 blocks cell proliferation, migration, wound repair, and network formation in vitro. This compound demonstrates efficacy in animal models of vascular leakage and angiogenesis (*45*, *46*) that have served as key platforms in the development of nAMD/DR therapies. BT2 prevented retinal vascular permeability in rats following choroidal laser injury as effectively as first-line therapy for nAMD and DME following six aflibercept injections compared with two of BT2 at the same dose. BT2 reduced

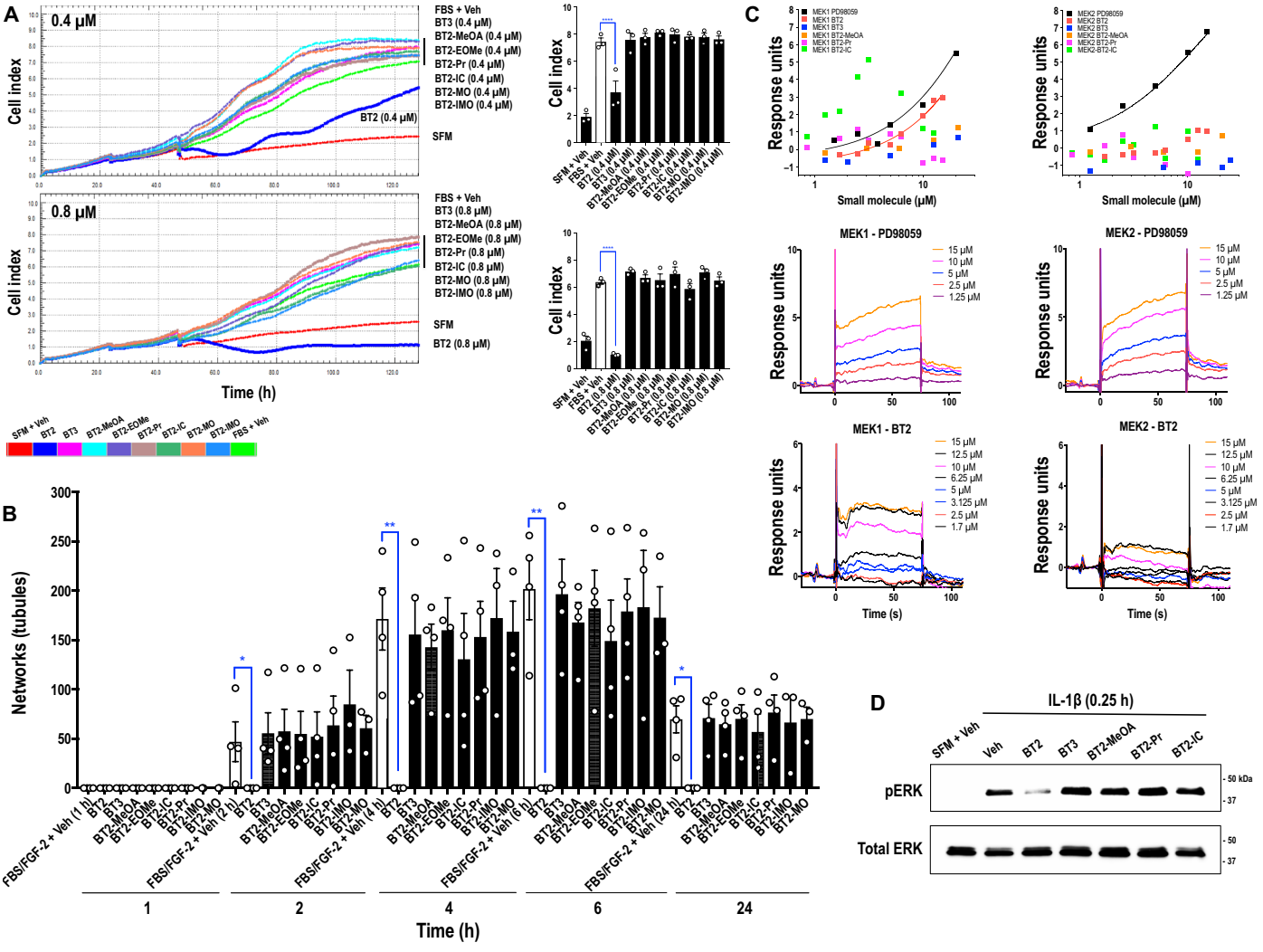

Fig. 5. Carbamate moiety in BT2 is critical to its interaction with MEK1 and functional effects. (**A**) Serum-deprived HMEC-1 cells were treated with compound (0.4 or 0.8 μM) in 5% FBS, and proliferation was monitored using xCELLigence. Left: Representative growth profiles from one experiment. Right: xCELLigence data representing means ± SEM of three independent experiments after 79 hours. One-way ANOVA or Mann-Whitney test. (**B**) HMEC-1 network formation in 1% FBS and FGF-2 (50 ng/ml) with compound (1 μM final) in Matrigel-coated wells. Networks quantified with NIH ImageJ. Data represent means ± SEM of three to four independent experiments. Kruskal-Wallis multiple comparisons test. (**C**) SPR analysis testing interaction of PD98059, BT2, and BT2 analogs with His-MEK1 (left) and His-MEK2 (right). Also shown are fits to equilibrium data for binding of PD98059 and BT2 to MEK1 (top left) and for binding of PD98059 to MEK2 (top right). Data were fitted using a simple Langmuir 1:1 binding isotherm in Biacore software. Measurements made on a Biacore T200 at 15°C in buffer comprising 20 mM Hepes, 150 mM NaCl, and 5% DMSO (pH 7.4). Data are representative of two independent experiments. (**D**) HMEC-1 cells were treated with 1 μM compound (BT2 and analogs) in serum-free medium for 4 hours. Medium was changed to IL-1β (20 ng/ml) with compound and incubated for 15 min. Western blotting was performed for pERK or total ERK. Data are representative of two biologically independent experiments. Approximate positions of molecular weight markers are shown. Where indicated, *$P < 0.05$, **$P < 0.01$, ****$P < 0.0001$.

CD31 staining in the IPL and INL, consistent with VEGF-A gain-of-function studies in amacrine and horizontal cells after studies that crossed *Ptf1a-Cre* mice with floxed *Vhl* (*Vhlf/f*) mice to induce pseudohypoxia revealed massive neovascularization in the IPL and INL (*47*). In rabbits, we found that BT2 inhibited retinal vascular leakiness induced by VEGF-A_{165}.

While BT2 suppressed the inducible expression of VEGF-A_{165}, its effects in the retina were not confined to VEGF. BT2 inhibited ERK activation and VCAM-1 expression, both implicated in the pathogenesis of nAMD and DR (*14*, *15*, *48*, *49*). Our findings suggest the existence of a pERK-FosB/ΔFosB-VCAM-1 cascade under conditions of cytokine stimulation. BT2 also inhibited a range of other genes involved in cell growth, migration, angiogenesis, and inflammation. BT2 is more potent than PD98059 and >40-fold more potent than curcumin, the main active ingredient in the golden spice turmeric that inhibits AP-1 (*50*) and is widely used for medicinal purposes despite double-blind placebo-controlled clinical trials of curcumin not having been successful (*22*).

We synthesized BT2 analogs bearing a variety of substitutions at the 2- and 10-positions of the 2-amino-dibenzo[b,f][1,4]oxazepin-11(10H)-one ring system. Minor variations of the carbamate moiety (BT2-MeOA and BT2-IC) markedly affected activity as did modifications at the 10-position (BT2-Pr, BT2-EOMe, BT2-MO, and BT2-IMO). We expected that BT2-EOMe, BT2-MO, and BT2-IMO, all of which

have lower calculated log Ps, would have increased water solubility. Although BT2-MeOA (and BT3) was more soluble than BT2, two separate assays revealed that BT2 remained the most biologically potent of all these compounds, indicating that larger substituents at the 2 and 10 positions are not advantageous. Comparison of BT2 with BT2-MeOA, which has the same molecular formula/weight and is an isomer of BT2 (linked through an amide), indicates that the carbamate moiety at the 2 position in BT2 is critical to BT2 function. BT2 may be amenable to lipid-based drug delivery systems, such as self-emulsifying delivery methodologies, that have improved oral absorption of poorly water-soluble drugs and facilitated high-dose toxicological studies (*51*).

Rodent and rabbit models are useful in recreating certain features of retinal disease in humans but may not totally recapitulate the human condition since nAMD and DR are complex, multifactorial chronic diseases that cannot be precisely recreated in acute experiments with a single stimulus (*52*). While rats offer advantages of rapid disease progression and comparative low cost, rats (like mice) do not have a macula (*53*). The size of the rabbit eye is more akin to the human eye, but its posterior segment circulation differs from primates and rodents, and rabbits also lack a macula (*54*). BT2 may overcome limitations in translatability that have hampered the broader use of humanized and species-specific reagents in animal models (*55*).

BT2 offers a new tool in the armamentarium targeting vascular permeability and angiogenesis. Unlike current clinically used protein-based therapies that solely target the VEGF system, BT2 inhibits multiple factors implicated in the pathogenesis of nAMD and DR. This compound might also serve as a tool in other disease or as a laboratory reagent inhibiting kinase-dependent signaling. The fact that BT2 retains stability and biological potency even after boiling or autoclaving and prolonged storage without refrigeration adds further to its pharmaceutical appeal.

MATERIALS AND METHODS

High-throughput screen of compound library

Hits were selected from the ~100,000 compound Lead Discovery Library at the HTS Facility at WEHI (Bundoora, VIC) with a commercially available human embryonic kidney 293 cell–based assay in 384-well microtiter plates in which Firefly luciferase was driven by multiple copies of the AP-1 response element (293/AP-1–luc cells, Panomics, Fremont, CA). Briefly, the cell-based assay involved plating 5×10^3 cells into 384-well plates in Dulbecco's modified Eagle's medium (DMEM; pH 7.4) containing 10% fetal bovine serum (FBS). After ~18 hours, the cells were induced with 2-*O*-tetradecanoylphorbol-13-acetate (10 ng/ml; Sigma, St. Louis, MO) in the absence or presence of test compound; then, after ~18 hours, luciferase activity was measured using a luminometer. The hit rate of the primary screen was 2.4%. Hits were picked for single-point retest in triplicate, and 931 test compounds were reconfirmed at greater than 50% inhibition. A substructure filter was then applied to remove pan-assay interference compounds, and using the most stringent filtering criteria, 256 hits were selected for further study. After dose-response testing, 24 compounds with molecular weight of <400 Da were reordered from suppliers and tested in secondary assays.

Compound synthesis and purification

BT2, Cpd B/X/LK001, and structural analogs were synthesized and purified (>95%) at Advanced Molecular Technologies Pty. Ltd. (Scoresby, VIC) or commercially obtained as indicated below.

(10-Ethyl-11-oxo-10,11-dihydro-dibenzo[b,f][1,4]oxazepin-2-yl)-carbamic acid ethyl ester (BT2)

Diethyl pyrocarbonate (22.2 ml, 24.43 g, 151 mmol) was added to 2-Amino-10-methyl-10H-dibenzo[b,f][1,4]oxazepin-11-one (BT3) (35.0 g, 137 mmol) in 100 ml of dimethylformamide (DMF), and the mixture was stirred for 1 hour under an atmosphere of nitrogen at 22°C. The solid was filtered and rinsed with ethyl acetate (EtOAc) (100 ml) to give a pure first crop. The combined solvent (DMF and EtOAc) was removed, and the mixture was dissolved in dichloromethane (DCM) (200 ml) and then washed twice with water (100 ml). The organic layer was separated, dried with $MgSO_4$, and filtered, and the solvent was removed to give a yellow solid. This solid was slurried in EtOAc and filtered to give a pure colorless solid. The crops were combined to give 35.0 g (79% yield) of a pure colorless solid. ^{1}H NMR (400 MHz, D_6-DMSO): δ = 1.15 to 1.40 (m, 6H), 4.05 to 4.25 (m, 4H), 7.20 (m, 3H), 7.30 (d, 1H), 7.48 (d, 1H), 7.55 (d, 1H), 7.50 (bs, 1H), and 9.70 (s, 1H) parts per million (ppm).

Isobutyl(10-ethyl-11-oxo-10,11-dihydrodibenzo[b,f][1,4] oxazepin-2-yl) carbamate (BT2-IC)

To 2-Amino-10-methyl-10H-dibenzo[b,f][1,4]oxazepin-11-one (1.5 g, 5.89 mmol, 1.0 eq) in 50 ml of DMF under an atmosphere of nitrogen was added diisobutyl dicarbonate (1.55 g, 7.08 mmol, 1.2 eq). The mixture was stirred overnight at 40°C (external). The solvent was removed, and the mixture was dissolved in DCM (200 ml) and washed twice with water (150 ml). Then, the organic layer was dried with $MgSO_4$ and filtered on a sintered funnel, and the solvent was removed to produce 3.0 g of a brown solid as a crude product. This solid was purified by column chromatography on silica gel using a mixture of hexane in ethyl acetate (starting from 10% ethyl acetate in hexane with polarity increased to 20%) to produce 1.55 g (74%) of a faint yellow solid as a product. ^{1}H NMR (400 MHz, $CDCl_3$): δ = 0.93 (s, 3H), 0.95 (s, 3H), 1.35 (t, 3H), 1.90 to 2.10 (m, 1H), 3.93 (d, 2H), 4.15 (q, 2H), 6.87 (s, 1H), 7.11 to 7.21 (m, 3H), 7.23 to 7.26 (m, 1H), 7.28 to 7.32 (m, 1H), 7.61 (d, 1H), and 7.75 (brs, 1H).

N-(10-ethyl-11-oxo-10,11-dihydro-dibenzo[b,f][1,4]oxazepin-2-yl)-2-methoxy-acetamide (BT2-MeOA)

To methoxy acetic acid (1.169 g, 0.996 ml, 12.9 mmol, 1.1 eq) in 60 ml of DMF under an atmosphere of nitrogen was added carbonyldiimidazole (2.487 g, 15.0 mmol, 1.3 eq). The mixture was stirred for 30 min. Then, the 2-amino-10-methyl-10H-dibenzo[b,f] [1,4] oxazepin-11-one (3.0 g, 11.8 mmol, 1.0 eq) was added, and the reaction was stirred at 30°C (external) overnight. The solvent was removed, and water (200 ml) and DCM (200 ml) were added to the mixture and acidified to pH 6 with 2 M HCl. The organic phase was washed twice with 50 ml of water. The organic layer was dried with $MgSO_4$ and filtered on a sintered funnel, and the solvent was removed to produce 3.7 g of a sticky yellow solid. The crude product was purified by column chromatography using 50% ethyl acetate in hexane to produce 3.26 g (85%) of a faint brown solid as a product. ^{1}H NMR (400 MHz, $CDCl_3$): δ = 1.22 (t, 3H), 3.35 (s, 3H), 3.95 (s, 2H), 4.10 (m, 2H), 7.20 to 7.30 (m, 3H), 7.35 (d, 1H), 7.52 (d, 1H), 7.80 (d, 1H), 8.03 (s, 1H), and 9.90 (s, 1H) ppm.

(11-Oxo-10-propyl-10,11-dihydro-dibenzo[b,f][1,4]oxazepin-2-yl)-carbamic acid ethyl ester (BT2-Pr)

To 2-Amino-10-propyl-10H-dibenzo[b,f][1,4]oxazepin-11-one (2.4 g, 9.43 mmol, 1.0 eq) in 70 ml of DMF under an atmosphere of nitrogen was added diethyl pyrocarbonate (2.30 g, 14.16 mmol, 1.5 eq). The mixture was stirred overnight at 40°C (external). The solvent was removed, and the mixture was dissolved in DCM

(200 ml) and washed twice with water (150 ml). The organic layer was separated and dried with $MgSO_4$ and filtered on a sintered funnel, and the solvent was removed to give 3.0 g of a brown solid as a crude product. This solid was purified by column chromatography using 20% ethyl acetate in hexane to produce 2.2 g (72%) of a faint yellow solid. ^{1}H NMR (400 MHz, $CDCl_3$): δ = 1.30 (t, 3H), 3.40 (s, 3H), 3.80(t, 2H), 4.20 to 4.25 (m, 4H), 6.60 (s, 1H), 7.13 to 7.26 (m, 5H), 7.55 to 7.60 (m, 2H), and 7.68 (s, 1H) ppm.

[10-(2-Methoxy-ethyl)-11-oxo-10,11-dihydro-dibenzo[b,f][1,4]oxazepin-2-yl]-carbamic acid ethyl ester (BT2-EOMe)

To 2-Amino-10-(2-methoxy-ethyl)-10H-dibenzo[b,f][1,4]oxazepin-11-one (2.9 g, 10.2 mmol, 1.0 eq) in 90 ml of DMF under an atmosphere of nitrogen was added diethyl pyrocarbonate (1.82 g, 11.22 mmol, 1.1 eq). The mixture was stirred overnight at 40°C (external). The solvent was removed, the mixture was dissolved in DCM (200 ml), and the organic phase was washed twice with water (150 ml). The organic layer was separated and dried with $MgSO_4$ and filtered on a sintered funnel, and the solvent was removed to produce 3.6 g of brown solid as a crude product. This solid was purified by column chromatography using 30% EtOAc in hexane to produce 3.5 g (96%) of a colorless solid. ^{1}H NMR (400 MHz, $CDCl_3$): δ = 1.30 (t, 3H), 3.40(s, 3H), 3.80(t, 2H), 4.20 to 4.25 (m, 4H), 6.60 (s, 1H), 7.13 to 7.26 (m, 5H), 7.55 to 7.60 (m, 2H), and 7.68 (s, 1H) ppm.

Ethyl (11-(oxetan-3-ylmethyl)dibenzo[b,f][1,4]oxazepin-2-yl)-carbamate and (BT2-IMO) and ethyl (10-(oxetan-3-ylmethyl)-11-oxo-10,11-dihydro-dibenzo[b,f][1,4]oxazepin-2-yl)-carbamate (BT2-MO)

First, 2-nitro-10H-dibenzo[b,f][1,4]oxazepin-11-one (3) (fig. S1B, scheme 3) (7.5 g, 0.029 mol, 1.0 eq) under an atmosphere of nitrogen was added to 100 ml of DMF and stirred for 5 min. Then, NaH [1.4 g, 2.34 g (60%) in oil, 0.058 mol, 2.0 eq] was added in small portions (an exotherm was observed). The mixture was stirred at 40°C (external) for 35 min. Then, oxetan-3-ylmethyl methanesulfonate (9.73 g, 0.058 mol, 2.0 eq) was added, and the reaction was stirred for 3 hours at 40°C (external). The reaction was followed by thin-layer chromatography in 20% ethyl acetate in hexane. When the reaction was complete, the solvent was removed on a kugel (100°C and full vacuum) (or on rotary evaporator using a strong pump ensuring bath temperature below 70°C), and then water (300 ml) was added. The solid was stirred with a spatula to make it precipitate in water. After filtration, the solid was dried in a vacuum oven overnight at 80°C. The crude product mixture was purified by column chromatography on silica gel using a mixture of hexane in ethyl acetate (starting from 20% ethyl acetate in hexane with polarity increased to 40%). The first band was the O-alkylated compound (RF = 0.65).

A 1.0 g (13% yield) of O-alkylated compound yield was obtained as a faint yellow solid. The melting point is 135° to 37°C (corrected). ^{1}H NMR (400 MHz, D_6-DMSO): δ = 3.42 to 3.57 (m, 1H), 4.53 (t, 2H), 4.65 (d, 2H), 4.74 to 4.79 (app. dd, 2H), 7.19 to 7.27 (m, 3H), 7.32 to 7.36 (m, 1H), 7.62 (d, 1H), 8.38 (d, 1H), and 8.47 (dd, 1H) ppm.

Second, O-alkyl. To 2-nitro-11-(oxetan-3-ylmethyl)dibenzo[b,f][1,4]oxazepin-11(10H)-one (1.5 g, 4.6 mmol, 1.0 eq) was added 50 ml of MeOH. The mixture was stirred at 40°C (external) for 15 min to dissolve all the solids. The reaction mixture was cooled to 22°C, and the flask was flushed with nitrogen. A 10% Pd/C (200 mg) was added, and the compound was hydrogenated at 40°C under an atmosphere of H_2 (external) for 1 hour. The solvent was removed to produce 1.2 g (98% yield) of a yellow solid, which was used for the next step without further purification (purity of ≥97%). The melting point is 150° to 152°C (corrected). ^{1}H NMR (400 MHz, D_6-DMSO): 4.48 to 4.60 (m, 4H), 4.72 to 4.78 (app. dd, 2H), 5.2 (s, 2H), 6.71 to 6.75 (m, 2H), 6.95 to 6.99 (m, 1H), 7.07 to 7.20 (m, 4H) ppm.

Last, O-Alkyl. To 2-amino-10-(oxetan-3-ylmethyl)dibenzo[b,f][1,4]oxazepin-11(10H)-one (1.2 g, 4.05 mmol, 1.0 eq) in 40 ml of DMF was added diethyl pyrocarbonate (0.98 g, 6.07 mmol, 1.5 eq). The mixture was stirred overnight at 40°C (external). The solvent was removed, and the mixture was dissolved in DCM (150 ml) and washed twice with water (150 ml). Then, the organic layer was dried with $MgSO_4$ and filtered on a sintered funnel, and the solvent was removed to produce 1.31 g of a faint yellow solid as a crude product. Crude product (1.3 g) was purified by column chromatography on silica gel using a mixture of hexane in ethyl acetate (starting from 20% ethyl acetate in hexane with polarity increased to 35%).

BT2-IMO

First, a 0.5 g (34% yield) was obtained as a colorless solid. The melting point is 159° to 162°C (corrected). ^{1}H NMR (400 MHz, $CDCl_3$): δ = 1.30 (t, 3 H), 3.47 to 3.59 (m, 1 H), 4.22 (q, 2H), 4.63 to 4.68 (m, 4H), 4.88 to 4.93 (m, 2 H), 6.60 (s, 1 H), 7.07 to 7.260 (m, 5 H), 7.50 to 7.59 (m, 2 H) ppm.

A 3.5 g of N-alkylated compound (48% yield) was obtained as a faint yellow solid. (RF = 0.45). The melting point is 106° to 109°C (corrected). ^{1}H NMR (400 MHz, D_6-DMSO): δ = 3.17 to 3.28 (m, 1 H), 4.29 (t, 2 H), 4.47 (br d, 2H), 4.53 to 4.58 (app. dd, 2H), 7.26 to 7.37 (m, 2H), 7.46 (dd, 1H), 7.57 to 7.64 (m, 2H), 8.40 (dd, 1 H), and 8.46 (d, 1 H) ppm.

Second, N-alkyl. To a 250 ml round bottom flask setup for hydrogenation was added to 2-nitro-10-(oxetan-3-ylmethyl)dibenzo[b,f][1,4]oxazepin-11(10H)-one (2.5 g, 6.12 mmol, 1.0 eq) and 50 ml of MeOH. The mixture was stirred at 40°C (external) for 15 min to dissolve all the solids. The flask was cooled to 22°C and flushed with nitrogen again. A 10% Pd/C (200 mg) was added, and the mixture stirrer under an atmosphere of hydrogen at 40°C (external) for 1 hour at atmospheric pressure. The mixture was filtered through celite, and the solvent was removed to yield a pure colorless solid (1.8 g, 99% yield) used for the next step without further purification. The melting point is 62° to 72°C (corrected). ^{1}H NMR (400 MHz, D_6-DMSO): δ = 3.11 to 3.22 (m, 1H), 4.26 (t, 2H), 4.53 (app. dd, 2H), 5.17 (br s, 2H), 7.67 (dd, 1H), 6.85 (d, 1H), 6.95 (d, 1H), 7.17 to 7.29 (m, 3H), and 7.49 (dd, 1H) ppm.

Last, N-alkyl. To 2-amino-10-(oxetan-3-ylmethyl)dibenzo[b,f][1,4]oxazepin-11(10OH)-one (1.6 g, 5.49 mmol, 1.0 eq) in 50 ml of DMF was added diethyl pyrocarbonate (1.44 g, 8.91 mmol, 1.5 eq). The mixture was stirred for 1 hour at 40°C (external). The solvent was removed, and the mixture was dissolved in DCM (150 ml) and washed twice with water (150 ml). The organic layer was dried with $MgSO_4$ and filtered on a sintered funnel, and the solvent was removed to produce the crude product, which was purified by column chromatography using 50% EtOAc in hexane. BT2-MO (1.91 g, 87% yield) was obtained as a colorless solid. The melting point is 161° to 162°C (corrected). ^{1}H NMR (400 MHz, $CDCl_3$): δ = 1.30 (t, 3H); 3.36 to 3.48 (m, 1H), 4.20 (q, 2H); 3.80 (t, 2H); 4.31 to 4.55 (m, 4 H); 4.70 to 4.76 (m, 2H), 6.65 (s, 1H), 7.13 to 7.26 (m, 5H), 7.57 (d, 1H), and 7.70 (s, 1H) ppm.

2-Methoxyethyl[[[4-(4-chlorobenzoyl)phenyl]amino]carbonyl] carbamate (Cpd B/X/LK001)

A solution of (4-amino-phenyl)-(4-chloro-phenyl)-methanone (49.1 g, 210 mmol) in DCM (150 ml) was cooled in an ice/NaCl bath at ~0°C (internal temperature). 2-Methoxyethyl carbonisocyanatidate

(40 g, 276 mmol) in DCM (150 ml) was added via a dropping funnel with the internal temperature being kept below 5°C. The ice bath was removed, and the solution was stirred for 1 hour at 22°C under nitrogen. The solution was filtered and the solid rinsed with methanol to give a pure faint yellow crop of desired product. A further crop was obtained by concentrating the filtrate (mixture of DCM and MeOH), filtration, and methanol wash. Fractions were combined to produce 49 g (62%) of the desired product. ^{1}H NMR (400 MHz, D_6-DMSO): δ = 10.52 (s, 1H, NH), 10.10 (s, 1H, NH), 7.75 to 7.68 (m, 6H), 7.62 (d, 2H), 4.80 (t, 2H), 3.58 (t, 2H), and 3.28 (s, 3H) ppm.

2-Methoxyethyl[[[4-(4-chlorophenyl)(hydroxyimino)methyl) phenyl]amino]carbonyl]carbamate (T4)

2-Methoxyethyl[[[4-(4-chlorobenzoyl)phenyl]amino]carbonyl] carbamate (20.7 g, 55 mmol), hydroxylamine hydrochloride (11.4 g, 165 mmol), and sodium acetate (13.5 g, 165 mmol) were stirred under a nitrogen atmosphere at reflux for 4 hours. The reaction mixture was filtered hot to remove any salts. The filtrate was cooled, and the product was filtered. The filtrate was concentrated by two-thirds, cooled to 22°C, and filtered to produce a second crop. The solid was vacuum dried at 60°C to give the desired product (15.8 g, 73%). ^{1}H NMR (400 MHz, D_6-DMSO) as a mixture of E and Z isomers (~1:1): δ = 11.43 (s, 0.46H, OH), 11.32 (s, 0.62H, OH), 10.42 (bs, 1H, NH), 9.90 (s, 0.49H, NH), 9.88 (s, 0.63H, NH), 7.59 (d, 0.94H), 7.52 (t, 2.44H), 7.42 (q, 1.92H), 7.35 to 7.25 (m, 3.44H), 4.28 (m, 2H), 3.58 (m, 2H), 3.27 (s, 1.28H), and 3.28 (s, 1.72H) ppm.

Ethyl (10-ethyl(2′,2′,2′-d3)-11-oxo-10,11-dihydrodibenzo[b,f] [1,4]oxazepin-2-yl)carbamate (BT2-deut)

First, 2-Nitro-10H-dibenzo[b,f][1,4]oxazepin-11-one (1 g, 3.9 mmol, 1 eq) was added to 10 ml of DMF and stirred for 5 min under nitrogen. Then, the NaH (187 mg, 0.32 g in oil, 7.8 mmol, 2 eq) was added in small portions. The mixture was stirred at 40°C external for 35 min. Then, ethyliodide-2,2,2-d3 (1.24 g, 0.62 ml, 7.8 mmol, 2 eq) was added and the reaction was stirred for 3 hours at 40°C external. The solvent was removed via evaporation and trituration three times with water returned a thick paste which was subjected to chromatography eluting using 15% EtOAc in hexane gave 10-(ethyl-2,2,2-d3)-2-nitrodibenzo[b,f][1,4]oxazepin-11(10H)-one as a yellow solid (0.42 g, 38%). The melting point is 142.3°C to 145.6°C (corrected). ^{1}H NMR (400 MHz, D_6-DMSO): δ = 4.12 (app s, 2H), 7.25 to 7.38 (m, 2H), 7.45 (dd, 1H), 7.60 (d and dd, 2H), 8.41 (dd, 1H), and 8.45 (d, 1H) ppm.

Second, 10-(ethyl-2,2,2-d3)-2-nitrodibenzo[b,f][1,4]oxazepin-11 (10H)-one (0.4 g, 1.41 mmol, 1 eq) and SnCl2 (0.8 g , 4.2 mmol, 3 eq) were dissolved in 10 ml of EtOH. The mixture was stirred at reflux for 2 hours. The solvent was removed and the mixture was dissolved in EtOAc (100 ml) and 1N NaOH aq. (50 ml). The organic phase was separated and washed with water (2 × 50 ml), dried with $MgSO_4$, filtered and the solvent evaporated. Chromatography eluting with 50% EtOAc in hexane gave the product 2-amino-10-(ethyl-2,2,2-d3) dibenzo[b,f][1,4]oxazepin-11(10H)-one as a faint beige solid (287 mg, 80%). The melting point is 165.5°C to 167.0°C (corrected). ^{1}H NMR (400 MHz, D_6-DMSO): δ = 4.0 (bq, 2H), 5.15 (s, 2H), 6.65 (dd, 1H), 6.84 (d, 1H), 6.95 (d, 1H), 7.15 to 7.30 (m, 3H), and 7.45 (dd, 1H) ppm.

Last, to 2-amino-10-(ethyl-2,2,2-d3)dibenzo[b,f][1,4] oxazepin-11(10H)-one (0.287 g, 1.2 mmol, 1 eq) in DMF (3 ml) was added diethyl pyrocarbonate (0.183 ml, 0.201 g, 1.24 mmol, 1.1 eq). The mixture was stirred for 1 hour under nitrogen at 25°C external. DMF was removed from the reaction mixture and the residual solid was triturated 3 times with EtOAc to give BT2-deut as a colorless solid (260 mg, 66%). The melting point is 184.3°C to 185.7°C (corrected). ^{1}H NMR (400 MHz, D_6-DMSO): δ =1.22 (t, 3H), 4.00 to 4.15 (q and br q, 4H), 7.2 to 7.3 (m, 3H), 7.35 (dd, 1H), 7.50 (dd, 1H), 7.58 (dd, 1H), 7.80 (d, 1H), and 9.75 (s, 1H) ppm.

Flubendazole (T6), 2-amino-10-ethyldibenzo[b,f][1,4]oxazepin-11 (10H)-one (BT3), and (4-Aminophenyl)(4-fluorophenyl) methanone (T7)

Flubendazole (T6), 2-amino-10-ethyldibenzo[b,f][1,4]oxazepin-11 (10H)-one (BT3), and (4-aminophenyl)(4-fluorophenyl)methanone (T7) are commercially available from AK Scientific Inc.

Cell culture

HMEC-1 cells were obtained from American Type Culture Collection (Rockville, MD) and grown in MCDB131 medium (Invitrogen, MD) (pH 7.4) supplemented with 10% FBS, hydrocortisone (1 μg/ml), epidermal growth factor (10 ng/ml), L-glutamine (2 mM), and penicillin/streptomycin. BAECs were obtained as primary cells from Cell Applications (San Diego, CA) and grown in DMEM (pH 7.4) supplemented with 10% FBS and antibiotics. BAECs were used in experiments between passages 4 and 6. Cells were routinely passaged after detachment with 0.05% trypsin/5 mM EDTA and maintain in a humidified atmosphere of 5% CO_2 at 37°C.

Western blot analysis with extracts of cells treated with serum

HMEC-1 cells (80 to 90% confluency) were arrested in serum-free MCDB131 medium without EGF or hydrocortisone for 20 hours. Cells were treated with 30 μM compound in serum-free MCDB131 medium for 4 hours, and the medium was changed to complete medium (with 10% FBS with EGF and hydrocortisone) with 30 μM compound for 1 hour. Total protein was harvested in radioimmunoprecipitation (RIPA) lysis buffer with protease inhibitors. Proteins were resolved on 4 to 20% (w/v) SDS–polyacrylamide gradient gels (Bio-Rad Mini-PROTEAN TGX) and transferred to Immobilon-P polyvinylidene difluoride (PVDF) membranes (Millipore, USA). Membranes were blocked with 5% skim milk and incubated with rabbit monoclonal FosB (1:1000; catalog no. 2251, Cell Signaling Technology, USA), rabbit monoclonal c-Fos antibodies (1:1000; catalog no. 2250, Cell Signaling Technology, USA) at 4°C overnight or mouse monoclonal β-actin antibodies (1:30,000; catalog no. A5316, Sigma-Aldrich) at 22°C for 15 min and then incubated with a horseradish peroxidase–conjugated secondary goat anti-rabbit (1:1000; catalog no. P0448, Dako Cytomation, Denmark) or goat anti-mouse (1:1000; catalog no. P0447, Dako Cytomation, Denmark) antibodies for 1 hour. Chemiluminescence was detected using the Western Lightning Chemiluminescence system (PerkinElmer, USA) and ImageQuant LAS 4000 biomolecular imager (GE Healthcare Life Sciences, USA). Band intensity in images generated with the LAS 4000 on automatic exposure with sensitivity/resolution setting high was quantified using National Institutes of Health (NIH) ImageJ.

Western blot analysis with extracts of cells treated with IL-1β

HMEC-1 cells (80 to 90% confluency) were arrested in serum-free MCDB131 medium (Invitrogen, MD) without any growth factor for 48 hours. Cells were treated with 30 μM compound in serum-free medium for 4 hours and incubated with IL-1β (20 ng/ml; catalog no. SRP3083, Sigma) in serum-free medium with the same concentration of compound for up to 4 hours, unless otherwise indicated. Total protein was harvested using RIPA buffer with protease inhibitors.

Proteins were resolved on 4 to 20% (w/v) SDS–polyacrylamide gradient gels and transferred to Immobilon-P PVDF membranes. Membranes were blocked with 5% skim milk and incubated with rabbit monoclonal FosB (1:1000; catalog no. 2251S, Cell Signaling Technology, USA), rabbit monoclonal VCAM-1 (1:1000; catalog no. 13662S, Cell Signaling Technology, USA), rabbit monoclonal p44/42 MAPK (1:1000; catalog no. 4695S, Cell Signaling Technology, USA), rabbit polyclonal p38 MAPK (1:1000; catalog no. 9212S, Cell Signaling Technology, USA), rabbit polyclonal SAPK/JNK (1:1000; catalog no. 9252S, Cell Signaling Technology, USA), rabbit monoclonal p-SAPK/JNK (1:1000; catalog no. 4671S, Cell Signaling Technology, USA), rabbit monoclonal p-p38 MAPK (1:1000; catalog no. 4511S, Cell Signaling Technology, USA), and mouse monoclonal phospho-p44/42 MAPK antibodies (1:2000; catalog no. 9106S, Cell Signaling Technology, USA) at 4°C overnight or mouse monoclonal β-actin antibodies (1:10,000; catalog no. A5316, Sigma-Aldrich) antibodies at 22°C for 1 hour. Membranes were then incubated with horseradish peroxidase–conjugated secondary goat anti-rabbit (1:1000; catalog no. P0448, Dako Cytomation, Denmark) or goat anti-mouse (1:1000; catalog no. P0447, Dako Cytomation, Denmark) antibodies for 1 hour. Chemiluminescence was detected using the Western Lightning Chemiluminescence system and ImageQuant LAS 4000 biomolecular imager. Band intensity in images generated with the LAS 4000 using the same settings were quantified by NIH ImageJ.

siRNA experiments

HMEC-1 cells (70 to 80% confluency) were arrested in serum-free MCDB131 medium with no hydrocortisone or EGF for 24 hours and transfected with nontargeting siRNA (catalog no. D-001810-10-50, Dharmacon, USA), FosB siRNA (catalog no. L-010086-01-0020, Dharmacon, USA), or VCAM-1 siRNA (catalog no. L-013351-00-0020, Dharmacon, USA) and Dharma FECT1 transfection reagent (catalog no. T-2001-03, Dharmacon, USA) mixed for 24 hours. siRNA experiments (with 0.6 μM FosB or 0.6 μM VCAM-1 siRNA) were performed shoulder-to-shoulder with nontargeting loading control siRNA at the same concentration. The cells were stimulated with IL-1β (20 ng/ml) in serum-free complete MCDB131 medium for a further 2 or 4 hours. Total protein was harvested using RIPA buffer with protease inhibitors and resolved on 4 to 20% (w/v) SDS–polyacrylamide gradient gels and transferred to Immobilon-P PVDF membranes. Membranes were blocked with 5% skim milk and incubated with rabbit monoclonal FosB (1:1000; catalog no. 2251S, Cell Signaling Technology, USA), rabbit monoclonal VCAM-1 (1:1000; catalog no. 13662S, Cell Signaling Technology, USA) at 4°C overnight, or mouse monoclonal β-actin (1:10,000; catalog no. A5316, Sigma-Aldrich) antibodies at 22°C for 1 hour. Membranes were incubated with horseradish peroxidase–conjugated secondary goat anti-rabbit (1:1000; catalog no. P0448, Dako Cytomation, Denmark) or goat anti-mouse (1:1000; catalog no. P0447, Dako Cytomation, Denmark) immunoglobulin (Ig) for 1 hour. Chemiluminescence was detected using the Western Lightning Chemiluminescence system and ImageQuant LAS 4000 biomolecular imager.

Plasmid overexpression

HMEC-1 cells were seeded into six-well plates, and at 70 to 80% confluency, the cells were deprived of serum (or EGF and hydrocortisone) overnight. Cells were transfected with 6 μg of the indicated plasmid [in pcDNA3.1$^+$/C-(K)DYK] (GenScript, USA) with Fugene 6 (Promega) according to manufacturer's protocol. Total protein lysates were collected 18, 24, 48, and 72 hours after plasmid transfection in RIPA buffer with protease inhibitors. Proteins were resolved on 4 to 20% (w/v) SDS–polyacrylamide gradient gels and transferred to Immobilon-P PVDF membranes. Membranes were blocked with 5% skim milk and incubated with rabbit monoclonal p44/42 MAPK (1:1000; catalog no. 4695S, Cell Signaling Technology), mouse monoclonal phospho-p44/42 MAPK (1:2000; catalog no. 9106S, Cell Signaling Technology), rabbit monoclonal FosB (1:1000; catalog no. 2251S, Cell Signaling Technology, USA), rabbit monoclonal VCAM-1 (1:1000; catalog no. 13662S, Cell Signaling Technology), or mouse monoclonal α-tubulin antibodies (1:40,000; catalog no. T5168, Sigma) at 4°C overnight. Membranes were then incubated with horseradish peroxidase–conjugated secondary goat anti-rabbit (1:1000; catalog no. P0448, Dako Cytomation, Denmark) or goat anti-mouse (1:1000; catalog no. P0447, Dako Cytomation, Denmark) antibodies for 1 hour. Chemiluminescence was detected using the Western Lightning Chemiluminescence system and ImageQuant LAS 4000 biomolecular imager.

RNA sequencing

HMEC-1 cells were seeded into nine 100-mm petri dishes with complete MCDB131 medium containing 10% FBS. At 70 to 80% confluency, cells were growth-arrested with serum-free MCDB131 medium with no hydrocortisone or EGF for 44 hours. Cells were pretreated with 30 μM BT2 in the same medium for 4 hours and then stimulated with IL-1β (20 ng/ml) for a further 4 hours. Total RNA was extracted using the RNeasy Mini Kit (Qiagen, Amtsgericht Düsseldorf) with modification. Briefly, cells were washed twice with precooled 1x phosphate-buffered saline (PBS), and TRIzol (Thermo Fisher Scientific, Waltham, MA) was added to lyze the cells. Chloroform was added to the mixture before centrifugation at 13,000 rpm for 15 min at 4°C. Upper aqueous layer containing total RNA was transferred to fresh microtubes, and isopropanol was added and loaded into RNeasy column. Columns were washed with buffers RW1 and RPE. Total RNA was eluted from the column using ribonuclease-free water. Samples were submitted to the Ramaciotti Centre for Genomics [University of New South Wales (UNSW), Australia] for TruSeq Stranded mRNA-seq preparation and sequencing by One NextSeq 500 1 × 75 bp high-output flowcell with data output up to 400 M reads. Quality control of samples was set at >80% higher than Q30 at 1 × 75 bp.

RNA-seq reads were first assessed for quality using the tool FastQC (v0.11.8) (www.bioinformatics.babraham.ac.uk/projects/fastqc/). The tool Salmon was used for quantifying transcript abundance from RNA-seq reads (*56*). The R package DESeq2 that incorporates a method for differential analysis of count data was then used to identify differentially expressed genes across specific comparisons (*57*). The heatmap.2 function from the R package gplots v3.0.1.1 was used to generate heat maps using counts per million values for sets of genes of interest. The Database for Annotation, Visualization and Integrated Discovery (DAVID) (*58*), a web-based online bioinformatics resource was used to identify the gene ontologies such as biological processes (BP) found to be enriched for lists of differentially expressed genes for specific comparisons.

Flow cytometry

HMEC-1 cells (at 80 to 90% confluency) were arrested in serum-free MCDB131 medium without EGF or hydrocortisone for 40 hours and

treated with 30 μM BT2 or BT3 for 4 hours. The cells were incubated in serum-free medium and exposed to IL-1β (20 ng/ml) with the same concentration of BT2 or BT3 for a further 4 hours. The cells were washed with PBS and then detached with Accutase (Stem Cell Technologies, catalog no. 07920). The cells were centrifuged at 300 g for 5 min and resuspended at 5×10^6 cells/ml containing BT2 or BT3. The cells were incubated with BV421-conjugated mouse anti-human CD106 (VCAM-1) (catalog no. 744309, BD) or BV421-conjugated mouse IgG_1 (catalog no. 562438, BD) for 45 min at 22°C. The cells were washed with a stain buffer, and the pellet was resuspended in 0.5 ml of 1% paraformaldehyde before flow cytometry BD FACSCanto II.

VCAM-1^+ and VCAM-1^- cells were gated by performing flow cytometry with or without primary VCAM-1 antibody (nonspecific staining), respectively. Representative gating from the latter (i.e., negative control) is shown as supplementary data (fig. S5, lower panels indicate minimal nonspecific staining). The gating strategy is based on fluorescence excitation of both the 488-nm laser and 405-nm laser with emission filters 670LP of 488 nm and 450/50 of 405 nm. Cells with autofluorescence or negative (blue population) had equal proportion of fluorescence in both channels, and VCAM-1^+ cells (red) emit light in the 450/50 filter.

Surface plasmon resonance

SPR was performed on a Biacore T200. The active and reference flow cells of a Xantec NIHMC Ni sensor chip were conditioned with 0.5 M NaEDTA followed by 5 mM $NiCl_2$ in immobilization buffer [20 mM Hepes and 150 mM NaCl (pH 7.4)]. Recombinant human His-MEK1 and His-MEK2 (500 nM; Thermo Fisher Scientific, catalog nos. PV3303 and PV3615, respectively) were injected for 15 min at 10 μl min^{-1} over separate active flow cells. All immobilization was carried out at 25°C. Following immobilization, the temperature was lowered to 15°C, and the buffer was changed to 20 mM Hepes, 150 mM NaCl, and 5% DMSO (pH 7.4). Samples of PD98059 (2.5 to 30 μM in running buffer) and BT2 (1.25 to 15 μM) were injected at a flow rate of 30 μl min^{-1} over immobilized MEK1 and MEK2. Solvent correction was applied to the data using a DMSO standard curve. Data were analyzed using the Biacore T200 Evaluation software. Before SPR, limits of compound solubility were determined using ^{1}H 1D NMR.

Endothelial proliferation assay using the xCELLigence System

HMEC-1 proliferation was evaluated using the xCELLigence System (Roche, Castle Hill). Briefly, HMEC-1 cells (5×10^3 cells per well) were seeded in a 96-well E-plate and inserted into the xCELLigence RTCA station (Roche). Cells were serum-deprived for 24 hours in MCDB131 medium, which contained EGF (10 ng/ml; Sigma-Aldrich) and hydrocortisone (1 μg/ml; Sigma-Aldrich), and then treated with compound (0.2 to 1 μM) in medium containing 5% FBS, EGF (10 ng/ml; Sigma-Aldrich), and hydrocortisone (1 μg/ml; Sigma-Aldrich). Cell growth was automatically monitored every 15 min by xCELLigence System. Cell index (CI) represents a quantitative measure of each well cell growth. In this system, CI is a unitless parameter that reports the impedance of electron flow caused by adherent cells.

Endothelial proliferation assay using the Countess system

HMEC-1 proliferation was assessed using a Countess II Automated Cell Counter (Thermo Fisher Scientific). Briefly, HMEC-1 cells (3×10^5 cells per well) were seeded in a 12-well plate. Cells were serum-deprived for 24 hours in MCDB131 medium, which contained EGF (10 ng/ml) and hydrocortisone (1 μg/ml) and then treated with compound (0.1 to 0.6 μM) in medium containing 5% FBS, EGF (10 ng/ml), and hydrocortisone (1 μg/ml). The cells were trypsinized after 24 hours and resuspended in complete medium, a 10 μl of aliquot was combined with an equal volume of 4% trypan blue, and total cell numbers and trypan blue–excluding cells as a proportion of total was determined using the Countess system.

Endothelial dual chamber migration assay

BAECs (at 6×10^3 cells per well) suspended in DMEM supplemented with 10% FBS were seeded into the upper chamber of 24-well plates fitted with Millicell cell culture inserts (catalog no. PI8P01250, Millipore). After 48 hours, the medium was changed to DMEM supplemented with 0.01% FBS, and the cells were incubated for 48 hours. Compounds prepared in DMEM containing 0.01% FBS were added to the upper chamber. VEGF-A_{165} (50 ng/ml; Sigma, catalog no. V7259) in medium containing 10% FBS was added to the lower chamber. After 24 hours, medium from the upper chamber was removed, and a cotton swab was used to remove nonmigrated cells and excess liquid. The insert was placed in 70% ethanol for 10 min to allow cell fixation, and membranes were dried for 10 to 15 min. Filters were excised and placed on slides. Mounting medium (Fluoroshield with 4′,6-diamidino-2-phenylindole; catalog no. F6057, Sigma) was added, and specimens were visualized using an EVOS FL microscope.

Endothelial repair following in vitro injury

HMEC-1 cells (at 90 to 100% confluency) in six-well plates were washed with PBS and treated with 0.6 μM compound in MCDB131 containing 5% FBS. A sterile pointed toothpick was used to scrape the cell monolayer, and the wells were photographed under 4× objective at 0 and 48 hours. Cell regrowth in the denuded zone was determined using Image-Pro Plus (Cybernetics, USA).

BT2 formulation analysis using RRLC-MS/MS

An RRLC-MS/MS method was developed under GLP by Iris Pharma using an Agilent 1200 Triple Quad G6410B to determine BT2 content in heat-treated or non–heat-treated BT2 formulations at 1 week (T1 week) or 6 weeks (T6 weeks) after preparation at room temperature. The formulations were heat (H)-treated (tubes placed in a 100°C water bath for 10 min) or non–heat-treated sonicated formulations of BT2 in saline containing 0.5% Tween 80 and 0.01% DMSO). Standard curves were constructed with eight concentrations between the lower limit of quantification (LLOQ) and the upper limit of quantification (ULOQ). Evaluations were performed on three preparations at the same dilution. Chromatograms were integrated using MassHunter software. For BT2 content analysis (T1 week and T6 weeks), calculation of mean, SD, coefficient of variation (%) and bias (%) were performed as follows: For T1, the theoretical concentration (i.e., the weighed/formulated material supplied) was used as reference to calculate the bias (%) of each preparation containing the test sample

$$\%\ \text{bias} = \frac{\text{Calculated Value–Theoretical Concentration}}{\text{Theoretical Concentration}} \times 100$$

Standard curves were fitted using Microsoft Exce1 2011. For each run, bias on back-calculated concentration of the standard curve and quality control was determined, with back-calculated concentrations of

the calibration standards being set within ±15% of the theoretical value, except for the LLOQ for which it was set within ±20%. At least 75% of the calibration standards, with a minimum of six, must have had to fulfill this criterion, and the coefficient of determination (R^2) was set at ≥0.98.

BT2 formulation analysis using LC-MS

DMSO (100 μl) and samples (~50 μl) were combined along with formic acid (1 μl). These solutions (10 μl) were further diluted with H_2O:CH_3CN (1:1) 0.1% formic acid (90 μl) for LC/MS analysis. Samples were separated by UPLC using an HPG−3400RS UPLC pump, autosampler, and column compartment system (Thermo Fisher Scientific, CA). Samples (0.1 μl) were loaded onto a Hypersil Gold aQ column (2.1 mm by 50 mm) containing 1.9-μm media (Thermo Fisher Scientific). Compounds were eluted using a linear gradient of H_2O:CH_3CN with A containing H_2O (0.1% formic acid) and B containing H_2O:CH_3CN (1:4, 0.1% formic acid). The gradient was T = 0 min, 2% B; T = 20 min, 75% B; T = 23 min, 95% B; T = 25 min, 95% B; T = 25.2 min, 2% B; and T = 30 min, 2% at 200 μl/min over 30 min. The column oven was heated to 45°C. Positive ions were generated by electrospray, and the QExactive Plus mass spectrometer (Thermo Fisher Scientific, Bremen, Germany) was operated in data-dependent acquisition mode. The heated electrospray ionization source was used with a high voltage of 3.8 kV applied, a vaporizer temp of 250°C, sheath gas of 20 U; aux gas of 5 U, and the heated capillary set to T = 290°C. A survey scan mass/charge ratio (m/z) 140 to 800 was acquired (resolution = 70,000 at m/z 200, with an AGC target value of 3×10^6 ions and maximum IT of 250 ms) with lockmass enabled (m/z 391.28429). Up to the 10 most abundant ions combining two microscans (with a minimum AGC target of 5×10^4 and maximum IT of 110 ms) were sequentially isolated (width m/z 1.8) and fragmented by HCD (NCE = 20, 30, 50) with an AGC target of 2×10^5 ions (resolution = 17,500 at m/z 200). m/z ratios selected for MS/MS were dynamically excluded for 12 s, and charge state exclusion was not enabled. LC/MS chromatograms were processed using Xcalibur Qual Browser Software.

Endothelial network formation assay

HMEC-1 cells (4×10^4 cells per well) in MCDB131 containing 1% FBS and compound (1 or 3 μM) or curcumin (1 to 40 μM) and fibroblast growth factor 2 (50 ng/ml) were added to 96-well plates coated overnight at 4°C with 100 μl of growth factor–reduced reconstituted basement membrane matrix (Matrigel, catalog no. 354230, Corning, NY). Network formation was observed over subsequent hours and photographed under 4× or 10× objective using an Olympus CKX41 microscope.

Matrigel plug assay

Matrigel (500 μl) containing VEGF-A_{165} (100 ng/ml), heparin (10 U), and BT2 or BT3 (2.5 mg per mouse) or its vehicle (saline containing 0.01% DMSO and 0.5% Tween 80) was subcutaneously injected into the left flanks of 8-week-old male C57BL/6 mice. After 7 days, the mice were euthanized by CO_2 asphyxiation, and the plugs were carefully removed. Formalin-fixed, paraffin-embedded sections were prepared from Matrigel plugs for immunohistological assessment. Heat-induced epitope retrieval was applied to all deparaffinized sections (4-μm Superfrost slides) in citrate buffer (pH 6) for 5 min at 110°C. Immunostaining for all groups with a given antibody was simultaneously performed, and development time was identical. Animal experiments were approved by the Animal Care and Ethics Committee at the UNSW.

For CD31 staining, sections were blocked with endogenous enzyme blocking agent (catalog no. S2003, Dako) for 10 min and then with 2% skim milk for 20 min. Slides were incubated with primary antibody rabbit polyclonal CD31 antibody (1:25; catalog no. ab28364, Abcam) for 1 hour at room temperature. Slides were rinsed with buffer and incubated with secondary antibody (goat anti-rabbit; catalog no. P0448, Dako) for 30 min, rinsed with buffer, incubated with diaminobenzidine chromogen (catalog no. K3468, Dako) for 5 min, and counterstained in hematoxylin and Scott blue. Slides were dehydrated in 100% ethanol and xylene and then coverslipped.

For FosB or VCAM-1 staining, sections were blocked with dual endogenous enzyme blocking agent (catalog no. S2003, Dako) for 10 min and then with 2% skim milk for 20 min. The slides were incubated with primary rabbit monoclonal FosB (catalog no. 2251, Cell Signaling Technology, USA) or rabbit polyclonal VCAM-1 (catalog no. sc-8304, Santa Cruz Biotechnology) for 1 hour at room temperature and then incubated for 10 min with the probe component of MACH3 Rabbit AP-Polymer Detection (Biocare Medical, M3R533 G, H, L). After rinsing with buffer, the slides were incubated with polymer component of MACH3 Rabbit AP-Polymer Detection (Biocare Medical, M3R533 G, H, L) for a further 10 min. The slides were incubated with red chromogen (Warp Red Chromogen Kit) for 7 min and counterstained in hematoxylin and Scott blue. The slides were dried using a filter paper and dehydrated in xylene and then coverslipped.

Slides were scanned using an Aperio ScanScope XT slide scanner (Leica Biosystems, Mt. Waverley, VIC, Australia), and images were captured using ImageScope software (Leica Biosystems). Positive intraplug staining was assessed using Image-Pro Plus software (Cybernetics, Bethesda, MD) in 5 to 12 randomly selected fields of view for each plug photographed under 10× (CD31), 20× (VCAM-1), and 40× (FosB) objectives and expressed as integrated optical density (IOD; the product of calibrated intensity (optical density) and area, i.e. IOD = intensity (mean) × area) (Media Cybernetics) (*59*). We also expressed positive immunostaining as the area of positive staining as a proportion (%) of plug area (*60*).

Rabbit retinal vascular hyperpermeability model

Male HY79b pigmented rabbits (8 to 12 weeks old) were anesthetized by an intramuscular injection of Rompun (xylazine)/Imalgene (ketamine). Compound (600 μg of BT2, BT3, or saline vehicle containing 0.5% Tween 80 and 10% DMSO vehicle in 100 μl) was injected into the right eye 5 days before rhVEGF-A_{165} induction. Injections were performed on anesthetized animals under an operating microscope using a 250-μl Hamilton syringe (fitted with 30-gauge needle). Retinal vascular permeability was induced by a single 50-μl intravitreal injection of 500 ng of rhVEGF-A_{165} (diluted in PBS with carrier protein) into the right eye. Forty-seven hours (±3 hours) after induction, sodium fluorescein (10% in saline, 50 mg/kg) was injected into the marginal ear vein. One hour after fluorescein injection, animals were anesthetized, and pupils were dilated by instillation of one drop of 0.5% tropicamide. Ocular fluorescence in both eyes was measured with a FM-2 Fluorotron Master ocular fluorophotometer. Animals were euthanized by injection of pentobarbital. The study was performed by Iris Pharma (La Gaude, France) with approval from the Animal Ethics Committee of Iris Pharma and the Animal Care and Ethics Committee at the UNSW.

Rat choroidal laser injury model

Male Brown Norway pigmented rats (8 to 14 weeks old) were anesthetized by an intramuscular injection of Rompun (xylazine)/Imalgene (ketamine). Pupils were dilated by instillation of one drop of 0.5% tropicamide before laser burn. Six burns were created in both eyes on day 0 by applying 170 mW of 532-nm laser light (Viridis laser, Quantel, France) on 75-μm spots around the optic nerve, between the main retinal vessel branches, for 0.1 s, through the slit lamp and contact lens. Production of a bubble at the time of laser application confirmed the rupture of Bruch's membrane. Compounds in vehicle (saline containing 0.01% DMSO and 0.5% Tween 80, sonicated) in 2 to 5 μl were intravitreally injected on days 0 and 7 under an operating microscope using a 30-gauge needle mounted on a 100-μl Hamilton syringe. Kenacort was intravitreally administered into each eye on day 0. Alternatively, aflibercept/Eylea in vehicle (saline) was intravitreally injected six times (days 0, 3, 7, 10, 14, and 17). Fluorescein angiography was performed using Heidelberg retinal angiography. After anesthesia, 10% sodium fluorescein (250 μl per 100 g of body weight) was subcutaneously injected, and ocular fluorescence was recorded 10 min after dye injection. Fluorescein leakage was evaluated on days 14 and 21 in the angiograms by two examiners masked to the study groups and graded for fluorescein intensity as follows: score 0, no leakage; 1, slightly stained; 2, moderately stained; 3, strongly stained. The studies were performed by Iris Pharma (La Gaude, France) with approval from the Animal Ethics Committee of Iris Pharma and the Animal Care and Ethics Committee at the UNSW.

Immunohistochemical staining of rat retina

Rabbit monoclonal anti-CD31 (catalog no. ab182981), rabbit monoclonal anti–VCAM-1 (catalog no. ab134047), and rabbit polyclonal anti–VEGF-A (catalog no. ab46154) were obtained from Abcam. Rabbit monoclonal phospho-p44/42 MAPK (pERK1/2, Thr^{202}/Tyr^{204}) (catalog no. 4370) and rabbit monoclonal FosB (catalog no. 2251) were obtained from Cell Signaling Technology. Formalin-fixed, paraffin-embedded sections were prepared from resected rat eyes. Heat-induced epitope retrieval was applied to all deparaffinized sections (4-μm Superfrost slides) with either citrate buffer (pH 6) (VEGF-A, pERK, and VCAM-1) or EDTA buffer (pH 9) (CD31) for 5 min at 110°C. Sections were blocked with dual endogenous enzyme blocking agent (catalog no. S2003, DAKO) for 10 min and then with 2% skim milk for 20 min. Slides were incubated with primary antibody for 60 min at room temperature and then for 10 min with the probe component of MACH3 Rabbit AP-Polymer Detection (Biocare Medical, catalog no. M3R533 G, H, L). After rinsing with buffer, the slides were incubated with the polymer component of MACH3 Rabbit AP-Polymer Detection (Biocare Medical, M3R533 G, H, L) for a further 10 min. Slides were incubated with red chromogen (Warp Red Chromogen Kit) for 7 min and counterstained in hematoxylin and Scott blue. Slides were dried with filter paper and dehydrated in xylene and then coverslipped. Immunostaining with a given antibody was performed for all groups at the same time. Immunostained slides were scanned using an Aperio ScanScope XT slide scanner (Leica Biosystems, Mt. Waverley, VIC, Australia), and images were captured using ImageScope software (Leica Biosystems). IOD of positive staining (red chromogen) was assessed for CD31, $VEGF\text{-}A_{165}$, pERK, FosB, and VCAM-1 using Image-Pro Plus software (Cybernetics, Bethesda, MD). IOD in IPL and INL was quantified for CD31, OPL to OS for $VEGF\text{-}A_{165}$, INL to ONL for pERK, GCL to OS for FosB, and OLM for VCAM-1 using Image-Pro Plus. In addition, we expressed positive immunostaining as area of positive staining relative to retinal tissue area (%) (*60*). On image selection for quantification, for the vehicle and BT2 groups, all wounds in two to four sections per eye were identified and photographed under 20× objective. In the untreated group, which had no injury, photographs of one to three sections per eye were taken under 20× objective. Staining was quantified with $n = 3$ to 6 per group. Where $VEGF\text{-}A_{165}$ gradient staining was assessed relative to the wound, immunostaining was assessed in 10 consecutive 100-μm boxes starting 150 μm (double-headed arrow) from the wound center with an IOD in each box quantified with Image-Pro Plus.

Statistics

Statistical analysis was performed as described in the legends using PRISM v7.0d, and differences were considered significant when $P < 0.05$. Where indicated, $^{*}P < 0.05$, $^{**}P < 0.01$, $^{***}P < 0.001$, and $^{****}P < 0.0001$.

SUPPLEMENTARY MATERIALS

Supplementary material for this article is available at http://advances.sciencemag.org/cgi/content/full/6/31/eaaz7815/DC1

View/request a protocol for this paper from *Bio-protocol*.

REFERENCES AND NOTES

1. N. Cheung, P. Mitchell, T. Y. Wong, Diabetic retinopathy. *Lancet* **376**, 124–136 (2010).
2. P. Mitchell, G. Liew, B. Gopinath, T. Y. Wong, Age-related macular degeneration. *Lancet* **392**, 1147–1159 (2018).
3. I. Klaassen, C. J. Van Noorden, R. O. Schlingemann, Molecular basis of the inner blood-retinal barrier and its breakdown in diabetic macular edema and other pathological conditions. *Prog. Retin. Eye Res.* **34**, 19–48 (2013).
4. B. Bahrami, M. Zhu, T. Hong, A. Chang, Diabetic macular oedema: Pathophysiology, management challenges and treatment resistance. *Diabetologia* **59**, 1594–1608 (2016).
5. R. S. Apte, D. S. Chen, N. Ferrara, VEGF in signaling and disease: Beyond discovery and development. *Cell* **176**, 1248–1264 (2019).
6. Diabetic Retinopathy Clinical Research Network, J. A. Wells, A. R. Glassman, A. R. Ayala, L. M. Jampol, L. P. Aiello, A. N. Antoszyk, B. Arnold-Bush, C. W. Baker, N. M. Bressler, D. J. Browning, M. J. Elman, F. L. Ferris, S. M. Friedman, M. Melia, D. J. Pieramici, J. K. Sun, R. W. Beck, Aflibercept, bevacizumab, or ranibizumab for diabetic macular edema. *N. Engl. J. Med.* **372**, 1193–1203 (2015).
7. Australian Government, Table 5(a): Top 50 PBS Drugs (Generic Name) Sorted by Highest Government Cost, 2017–18. Summary of Pharmaceutical Benefits Scheme 2017–2018, (2018); www.pbs.gov.au/info/statistics/expenditure-prescriptions/expenditure-prescriptions-twelve-months-to-30-june-2018.
8. S. Rofagha, R. B. Bhisitkul, D. S. Boyer, S. R. Sadda, K. Zhang; SEVEN-UP Study Group, Seven-year outcomes in ranibizumab-treated patients in ANCHOR, MARINA, and HORIZON: A multicenter cohort study (SEVEN-UP). *Ophthalmology* **120**, 2292–2299 (2013).
9. V. H. Gonzalez, J. Campbell, N. M. Holekamp, S. Kiss, A. Loewenstein, A. J. Augustin, J. Ma, A. C. Ho, V. Patel, S. M. Whitcup, P. U. Dugel, Early and long-term responses to anti–vascular endothelial growth factor therapy in diabetic macular edema: Analysis of protocol I data. *Am. J. Ophthalmol.* **172**, 72–79 (2016).
10. J. Hess, P. Angel, M. Schorpp-Kistner, AP-1 subunits: Quarrel and harmony among siblings. *J. Cell Sci.* **117**, 5965–5973 (2004).
11. T. Oshitari, S. Yamamoto, S. Roy, Increased expression of c-Fos, c-Jun and c-Jun N-terminal kinase associated with neuronal cell death in retinas of diabetic patients. *Curr. Eye Res.* **39**, 527–531 (2014).
12. M. Mishra, J. Flaga, R. A. Kowluru, Molecular mechanism of transcriptional regulation of matrix metalloproteinase-9 in diabetic retinopathy. *J. Cell. Physiol.* **231**, 1709–1718 (2016).
13. Y. Subhi, M. Krogh Nielsen, C. R. Molbech, A. Oishi, A. Singh, M. H. Nissen, T. L. Sørensen, Plasma markers of chronic low-grade inflammation in polypoidal choroidal vasculopathy and neovascular age-related macular degeneration. *Acta Ophthalmol.* **97**, 99–106 (2019).
14. S. V. Kyosseva, Targeting MAPK signaling in age-related macular degeneration. *Ophthalmol. Eye Dis.* **8**, 23–30 (2016).

15. J. B. Jonas, Y. Tao, M. Neumaier, P. Findeisen, Monocyte chemoattractant protein 1, intercellular adhesion molecule 1, and vascular cell adhesion molecule 1 in exudative age-related macular degeneration. *Arch. Ophthalmol.* **128**, 1281–1286 (2010).
16. T. Khalfaoui, G. Lizard, A. Ouertani-Meddeb, Adhesion molecules (ICAM-1 and VCAM-1) and diabetic retinopathy in type 2 diabetes. *J. Mol. Histol.* **39**, 243–249 (2008).
17. Y. Mitamura, A. Okumura, C. Harada, K. Namekata, K. Nakamura, A. Tashimo, K. Ohtsuka, T. Harada, Activator protein-1 in epiretinal membranes of patients with proliferative diabetic retinopathy. *Diabetologia* **49**, 209–211 (2006).
18. J. Jia, T. Ye, P. Cui, Q. Hua, H. Zeng, D. Zhao, AP-1 transcription factor mediates VEGF-induced endothelial cell migration and proliferation. *Microvasc. Res.* **105**, 103–108 (2016).
19. A. Damert, E. Ikeda, W. Risau, Activator-protein-1 binding potentiates the hypoxia-inducible factor-1-mediated hypoxia-induced transcriptional activation of vascular-endothelial growth factor expression in C6 glioma cells. *Biochem. J.* **327**, 419–423 (1997).
20. E. J. Nestler, ΔFosB: A transcriptional regulator of stress and antidepressant responses. *Eur. J. Pharmacol.* **753**, 66–72 (2015).
21. J. B. Baell, G. A. Holloway, New substructure filters for removal of pan assay interference compounds (PAINS) from screening libraries and for their exclusion in bioassays. *J. Med. Chem.* **53**, 2719–2740 (2010).
22. K. M. Nelson, J. L. Dahlin, J. Bisson, J. Graham, G. F. Pauli, M. A. Walters, The essential medicinal chemistry of curcumin. *J. Med. Chem.* **60**, 1620–1637 (2017).
23. A. Krebs, H. Hagemann, Verfahren zur Herstellung von Alkoxycarbonylisocyanten, European Patent Office EP0230224B1 (1991).
24. L. Marconcini, S. Marchiò, L. Morbidelli, E. Cartocci, A. Albini, M. Ziche, F. Bussolino, S. Oliviero, *c-fos*-induced growth factor/vascular endothelial growth factor D induces angiogenesis in vivo and in vitro. *Proc. Natl. Acad. Sci. U.S.A.* **96**, 9671–9676 (1999).
25. R. Shao, X. Guo, Human microvascular endothelial cells immortalized with human telomerase catalytic protein: A model for the study of in vitro angiogenesis. *Biochem. Biophys. Res. Commun.* **321**, 788–794 (2004).
26. S. Lamy, D. Gingras, R. Béliveau, Green tea catechins inhibit vascular endothelial growth factor receptor phosphorylation. *Cancer Res.* **62**, 381–385 (2002).
27. S. Hussain, M. Slevin, M. A. Mesaik, M. I. Choudhary, A. H. Elosta, S. Matou, N. Ahmed, D. West, J. Gaffney, Cheiradone: A vascular endothelial cell growth factor receptor antagonist. *BMC Cell Biol.* **9**, 7 (2008).
28. I. Arnaoutova, J. George, H. K. Kleinman, G. Benton, The endothelial cell tube formation assay on basement membrane turns 20: State of the science and the art. *Angiogenesis* **12**, 267–274 (2009).
29. P. A. Campochiaro, Ocular neovascularization. *J. Mol. Med.* **91**, 311–321 (2013).
30. X. Ju, X. Yang, T. Yan, H. Chen, Z. Song, Z. Zhang, W. Wu, Y. Wang, EGFR inhibitor, AG 1478, inhibits inflammatory infiltration and angiogenesis in mice with diabetic retinopathy. *Clin. Exp. Pharmacol. Physiol.* **46**, 75–85 (2019).
31. X. Wang, X. Xu, L. Tang, S. P. Song, C. Fan, Interactions between endostatin and vascular endothelial growth factor (VEGF) and inhibition of choroidal neovascularization. *Int. J. Mol. Sci.* **8**, 61–69 (2007).
32. G. Foureaux, B. S. Nogueira, D. C. O. Coutinho, M. K. Raizada, J. C. Nogueira, A. J. Ferreira, Activation of endogenous angiotensin converting enzyme 2 prevents early injuries induced by hyperglycemia in rat retina. *Braz. J. Med. Biol. Res.* **48**, 1109–1114 (2015).
33. M. Puhlmann, D. M. Weinreich, J. M. Farma, N. M. Carroll, E. M. Turner, H. R. Alexander Jr., Interleukin-1β induced vascular permeability is dependent on induction of endothelial tissue factor (TF) activity. *J. Transl. Med.* **3**, 37 (2005).
34. S. A. Vinores, W.-H. Xiao, J. Shen, P. A. Campochiaro, TNF-α is critical for ischemia-induced leukostasis, but not retinal neovascularization nor VEGF-induced leakage. *J. Neuroimmunol.* **182**, 73–79 (2007).
35. N. Dong, B. Xu, L. Chu, X. Tang, Study of 27 aqueous humor cytokines in type 2 diabetic patients with or without macular edema. *PLOS ONE* **10**, e0125329 (2015).
36. M. Takeda, A. Takamiya, A. Yoshida, H. Kiyama, Extracellular signal-regulated kinase activation predominantly in Müller cells of retina with endotoxin-induced uveitis. *Invest. Ophthalmol. Vis. Sci.* **43**, 907–911 (2002).
37. A. Caicedo, D. G. Espinosa-Heidmann, Y. Piña, E. P. Hernandez, S. W. Cousins, Blood-derived macrophages infiltrate the retina and activate Muller glial cells under experimental choroidal neovascularization. *Exp. Eye Res.* **81**, 38–47 (2005).
38. M. Makhoul, R. Dewispelaere, L. J. Relvas, V. Elmaleh, L. Caspers, C. Bruyns, F. Willermain, Characterization of retinal expression of vascular cell adhesion molecule (VCAM-1) during experimental autoimmune uveitis. *Exp. Eye Res.* **101**, 27–35 (2012).
39. M. Khoder, H. Abdelkader, A. ElShaer, A. Karam, M. Najlah, R. G. Alany, The use of albumin solid dispersion to enhance the solubility of unionizable drugs. *Pharm. Dev. Technol.* **23**, 732–738 (2018).
40. D. T. Dudley, L. Pang, S. J. Decker, A. J. Bridges, A. R. Saltiel, A synthetic inhibitor of the mitogen-activated protein kinase cascade. *Proc. Natl. Acad. Sci. U.S.A.* **92**, 7686–7689 (1995).
41. F. S. Jones, The effect of heat on antibodies. *J. Exp. Med.* **46**, 291–301 (1927).
42. Comparison of Age-related Macular Degeneration Treatments Trials (CATT) Research Group, M. G. Maguire, D. F. Martin, G.-S. Ying, G. J. Jaffe, E. Daniel, J. E. Grunwald, C. A. Toth, F. L. Ferris, S. L. Fine, Five-year outcomes with anti–vascular endothelial growth factor treatment of neovascular age-related macular degeneration: The comparison of age-related macular degeneration treatments trials. *Ophthalmology* **123**, 1751–1761 (2016).
43. A. C. Pedrosa, A. Reis-Silva, J. Pinheiro-Costa, J. Beato, P. Freitas-da-Costa, M. S. Falcão, F. Falcão-Reis, Â. Carneiro, Treatment of neovascular age-related macular degeneration with anti-VEGF agents: Retrospective analysis of 5-year outcomes. *Clin. Ophthalmol.* **10**, 541–546 (2016).
44. F. G. Holz, R. Tadayoni, S. Beatty, A. Berger, M. G. Cereda, R. Cortez, C. B. Hoyng, P. Hykin, G. Staurenghi, S. Heldner, T. Bogumil, T. Heah, S. Sivaprasad, Multi-country real-life experience of anti–vascular endothelial growth factor therapy for wet age-related macular degeneration. *Br. J. Ophthalmol.* **99**, 220–226 (2015).
45. C. K. Pan, C. Durairaj, U. B. Kompella, O. Agwu, S. C. Oliver, H. Quiroz-Mercado, N. Mandava, J. L. Olson, Comparison of long-acting bevacizumab formulations in the treatment of choroidal neovascularization in a rat model. *J. Ocul. Pharmacol. Ther.* **27**, 219–224 (2011).
46. H. Ameri, G. J. Chader, J.-G. Kim, S. R. Sadda, N. A. Rao, M. S. Humayun, The effects of intravitreous bevacizumab on retinal neovascular membrane and normal capillaries in rabbits. *Invest. Ophthalmol. Vis. Sci.* **48**, 5708–5715 (2007).
47. Y. Usui, P. D. Westenskow, T. Kurihara, E. Aguilar, S. Sakimoto, L. P. Paris, C. Wittgrove, D. Feitelberg, M. S. Friedlander, S. K. Moreno, M. I. Dorrell, M. Friedlander, Neurovascular crosstalk between interneurons and capillaries is required for vision. *J. Clin. Invest.* **125**, 2335–2346 (2015).
48. X. Ye, H. Ren, M. Zhang, Z. Sun, A. C. Jiang, G. Xu, ERK1/2 signaling pathway in the release of VEGF from Müller cells in diabetes. *Invest. Ophthalmol. Vis. Sci.* **53**, 3481–3489 (2012).
49. G. R. Barile, S. S. Chang, L. S. Park, V. S. Reppucci, W. M. Schiff, A. M. Schmidt, Soluble cellular adhesion molecules in proliferative vitreoretinopathy and proliferative diabetic retinopathy. *Curr. Eye Res.* **19**, 219–227 (1999).
50. N. Ye, Y. Ding, C. Wild, Q. Shen, J. Zhou, Small molecule inhibitors targeting activator protein 1 (AP-1). *J. Med. Chem.* **57**, 6930–6948 (2014).
51. X.-Q. Chen, T. Ziemba, C. Huang, M. Chang, C. Xu, J. X. Qiao, T. C. Wang, H. J. Finlay, M. E. Salvati, L. P. Adam, O. Gudmundsson, M. J. Hageman, Oral delivery of highly lipophilic, poorly water-soluble drugs: Self-emulsifying drug delivery systems to improve oral absorption and enable high-dose toxicology studies of a cholesteryl ester transfer protein inhibitor in preclinical species. *J. Pharm. Sci.* **107**, 1352–1360 (2018).
52. R. Robinson, V. A. Barathi, S. S. Chaurasia, T. Y. Wong, T. S. Kern, Update on animal models of diabetic retinopathy: From molecular approaches to mice and higher mammals. *Dis. Model. Mech.* **5**, 444–456 (2012).
53. M. E. Pennesi, M. Neuringer, R. J. Courtney, Animal models of age related macular degeneration. *Mol. Aspects Med.* **33**, 487–509 (2012).
54. S. Chen, N. A. Popp, C.-C. Chan, Animal models of age-related macular degeneration and their translatability into the clinic. *Expert Rev. Opthalmol.* **9**, 285–295 (2014).
55. F. Lu, R. A. Adelman, Are intravitreal bevacizumab and ranibizumab effective in a rat model of choroidal neovascularization? *Graefes Arch. Clin. Exp. Ophthalmol.* **247**, 171–177 (2009).
56. R. Patro, G. Duggal, M. I. Love, R. A. Irizarry, C. Kingsford, Salmon provides fast and bias-aware quantification of transcript expression. *Nat. Methods* **14**, 417–419 (2017).
57. M. I. Love, W. Huber, S. Anders, Moderated estimation of fold change and dispersion for RNA-seq data with DESeq2. *Genome Biol.* **15**, 550 (2014).
58. X. Jiao, B. T. Sherman, D. W. Huang, R. Stephens, M. W. Baseler, H. C. Lane, R. A. Lempicki, DAVID-WS: A stateful web service to facilitate gene/protein list analysis. *Bioinformatics* **28**, 1805–1806 (2012).
59. H. Liu, Z. Shen, Z. Wang, X. Wang, H. Zhang, J. Qin, X. Qin, J. Xu, Y. Sun, Increased expression of IDO associates with poor postoperative clinical outcome of patients with gastric adenocarcinoma. *Sci. Rep.* **6**, 21319 (2016).
60. J.-Y. Kim, J. Leem, E. J. Jeon, Protective effects of melatonin against aristolochic acid-induced nephropathy in mice. *Biomolecules* **10**, 11 (2020).

Acknowledgments: We acknowledge the facilities and scientific and technical assistance of the Biomedical Imaging Facility and Flow Cytometry Facility at Mark Wainwright Analytical Centre (UNSW) and, in particular, F. Shang for immunohistochemical staining and C. Brownlee for flow cytometry advice and analysis; I. Street, J. Baell, J. Parisot, K. Lackovic, and S. Sovath (WEHI) for helpful assistance during the high-throughput chemical screen; the Bosch Molecular Biology Facility at the University of Sydney for providing access to SPR infrastructure; and I. Dawes (UNSW) for critical review of the manuscript. **Funding:** This work was supported by grants from the National Health and Medical Research Council of Australia (NHMRC) and Cancer Institute New South Wales (CINSW). **Author contributions:** L.M.K. originally conceived, designed, and led the project; interpreted the data; and drafted the article. Y.L., A.M.N.A., M.-C.Y., M.E., F.S.S., B.W., L.E.W.-W., E.C., S.I., L.P.-L., and M.J.R. designed and performed experiments and analyzed and interpreted the data. N.P.D. conducted

bioinformatics analyses. J.M. and R.D.J. performed chemical synthesis and analyzed and interpreted the compound data. M.Z., S.J.A., A.C., and P.M. analyzed and/or interpreted the ocular data. F.B. and K.V.-Q. directed the rabbit and rat ocular experiments and analyzed and interpreted the data. J.S. performed and oversaw statistical analyses. J.P.M. analyzed and interpreted the SPR data. S.M.M. designed the chemical synthesis strategy and interpreted the compound data. All authors read and/or critically revised and approved the article.
Competing interests: A.C. and P.M. have consulted for Bayer, Novartis, and Allergan. The other authors report no competing interests. NewSouth Innovations Pty. Ltd. (UNSW) filed a provisional patent application related to this work. **Data and materials availability:** All data needed to evaluate the conclusions in the paper are present in the paper and/or the Supplementary Materials.

Submitted 8 October 2019
Accepted 16 June 2020
Published 29 July 2020
10.1126/sciadv.aaz7815

Citation: Y. Li, A. M. N. Alhendi, M.-C. Yeh, M. Elahy, F. S. Santiago, N. P. Deshpande, B. Wu, E. Chan, S. Inam, L. Prado-Lourenco, J. Marchand, R. D. Joyce, L. E. Wilkinson-White, M. J. Raftery, M. Zhu, S. J. Adamson, F. Barnat, K. Viaud-Quentric, J. Sockler, J. P. Mackay, A. Chang, P. Mitchell, S. M. Marcuccio, L. M. Khachigian, Thermostable small-molecule inhibitor of angiogenesis and vascular permeability that suppresses a pERK-FosB/ΔFosB–VCAM-1 axis. *Sci. Adv.* **6**, eaaz7815 (2020).

Science Advances

Thermostable small-molecule inhibitor of angiogenesis and vascular permeability that suppresses a pERK-FosB/ ΔFosB–VCAM-1 axis

Yue Li, Ahmad M. N. Alhendi, Mei-Chun Yeh, Mina Elahy, Fernando S. Santiago, Nandan P. Deshpande, Ben Wu, Enoch Chan, Shafqat Inam, Leonel Prado-Lourenco, Jessica Marchand, Rohan D. Joyce, Lorna E. Wilkinson-White, Mark J. Raftery, Meidong Zhu, Samuel J. Adamson, François Barnat, Karen Viaud-Quentric, Jim Sockler, Joel P. Mackay, Andrew Chang, Paul Mitchell, Sebastian M. Marcuccio and Levon M. Khachigian

Sci Adv **6** (31), eaaz7815.
DOI: 10.1126/sciadv.aaz7815

Science Advances (ISSN 2375-2548) is published by the American Association for the Advancement of Science, 1200 New York Avenue NW, Washington, DC 20005. The title *Science Advances* is a registered trademark of AAAS.